Multipatch isogeometric mortar methods for thick shells

Nicolas Adam, Patrick Le Tallec, Malek Zarroug

Highlights

Multipatch isogeometric mortar methods for thick shells

Nicolas Adam,Patrick Le Tallec,Malek Zarroug

- Modelisation of multipatch Reissner-Mindlin isogeometric shells.
- Development of industrially oriented coupling strategies combining mortar discretisations and augmented lagrangian formulations.
- Theoretical and practical assessment of convergence of mortar methods for isogeometric shells with cross point modifications
- Development and extension of reduced quadrature rules for surface and interface integrals
- Numerical validations on academic and industrial examples, including problems with geometrically non-conforming interfaces.

Multipatch isogeometric mortar methods for thick shells

Nicolas Adam[a,b], Patrick Le Tallec[a] and Malek Zarroug[b]

[a]Laboratoire de Mécanique des Solides (CNRS UMR 7649), École Polytechnique, Route de Saclay, 91128 Palaiseau, France
[b]Direction Scientifique et Technologies Futures, Groupe PSA, Route de Gisy, 78140 Vélizy-Villacoublay, France

ARTICLE INFO

Keywords:
Multipatch isogeometric analysis
Reissner-Mindlin shells
Reduced integration
Mortar methods
Convergence assessment

ABSTRACT

This paper introduces, analyzes and validates isogeometric mortar methods for the solution of thick shells problems which are set on a multipatch geometry. A particular attention will be devoted to the introduction of a proper formulation of the coupling conditions, with a particular interest on augmented lagrangian formulations, to the choice and validation of mortar spaces, and to the derivation of adequate integration rules. The relevance of the proposed approach is assessed numerically on various significative examples.

1. Introduction

The concept of isogeometric analysis (IGA) was first proposed by Hughes et al. in [1]. A considerable advantage of the method is to keep the same geometry, constructed in a computer-aided design (CAD) software, for the analysis step. This is possible by the use of the same shape functions for design and for analysis. Consequently, the kinematic quantities can be precisely evaluated without introducing an error due to the spatial discretization of the underlying geometry. More details on isogeometric methods can be found in [2].

Geometries constructed in a CAD software are generally comprised of several domains, which are also called patches, defined with B-splines or non-uniform rational B-splines (NURBS) shape functions. A comprehensive study of the numerical implementation of NURBS functions is given in [3]. The patches can be trimmed, if they cannot be constructed by a tensor product of basis functions, or untrimmed if they can be meshed exclusively with quadrangular elements. Analysis of trimmed structures [4–7] is recent and can lead to various difficulties such as element integration or weak condition enforcement. In this study, we will only focus on complex multipatch untrimmed geometries which require a robust treatment of continuity conditions between domains. This work then concerns industrial parts that can be represented by structures such as plates or shells for which the effects of transverse shear cannot be neglected. For this purpose, Reissner-Mindlin model was retained and rotationnal degrees of freedom (DOF) of the normal will be taken into account.

Literature is particularly rich concerning domain coupling in IGA for thin plate or shell structures. For conforming meshes, Kiendl et al. [8] proposed to add a fictitious bending strip to transfer the bending moment and keep a C^0 continuity between patches. Another method for a C^0/G^1 continuity consists in a virtual projection of control points for each interface (Oslo algorithm [9]) associated with a static condensation method or penalty method, see [10]. A Nitsche-based formulation was proposed in [11], for plane problems or for 3D problems [12], which can preserve uniqueness of the solution at the cost of an additional eigenvalues problem to solve.

It is well-known that mortar method is an interesting alternative to enforce contact or continuity conditions in coupling problems [13–17]. In this case, the choice of the dual space is essential. From a theoretical point of view, the space of the Lagrange multipliers has to satisfy two conditions. The first is the inf-sup stability and the other one is to achieve a good approximation of the dual space. Noting by p the order of the primal space splines functions, a dual space of order $p/p-1/p-2$ was proposed by Brivadis et al. [18]. Here we will present a mortar method with a simplified dual space of order p which can be easily applied to industrial parts at a low computational cost.

Therefore, the purpose of the present paper is to introduce, analyze and validate isogeometric mortar methods for solving thick shells problems which are set on a multipatch defined geometry. A particular attention will be devoted to the introduction of a proper formulation of the coupling conditions, with a particular interest on augmented lagrangian formulations, to the choice of mortar spaces, and to the derivation of adequate integration rules.

This article is structured in six main sections. Section 2 presents a brief review of the shape functions used in isogeometric methods. Section 3 introduces the Reissner-Mindlin shell model to be used herein. In Section 4 the

ORCID(s):

multipatch problem and a functional and discretization framework will be given. Convergence results will be reviewed and adapted in Section 5 and integration rules will be discussed in 6. Finally, some numerical results are proposed on academic and industrial parts in Section 7.

2. Shape functions in isogeometric analysis

Let us recall that a knot vector is a non-decreasing set of real numbers $\Xi = \left\{\xi_1, \dots, \xi_{n+p+1}\right\}$ which represent coordinates in the parameter space. The first and last entries in Ξ are repeated $p+1$ times which means that we use herein an open knot vector. Open knot vectors are widely used in CAD software and guarantee that basis functions are interpolatory at the ends of the parameter segment. We also define the breakpoint vector, i.e., the vector Ξ^* corresponding to Ξ without any repetitions, which splits the parameter space into elements and so define a mesh. B-splines are then piecewise polynomial functions N_i^p which are recursively built on Ξ [3] . These functions generate the spline space $S^p(\Xi) = \text{span}\left\{N_i^p(\xi),\ i = 1, \dots, n\right\}$ of order p known to have excellent approximation properties. Moreover, each function N_i^p is a piecewise positive polynomial of order p and has a compact support such that $N_i^p \geq 0$ within the knot interval $[\xi_i, \dots, \xi_{i+p+1}[$. The regularity between each element is C^{p-m_j} and so depends on the corresponding knot multiplicity m_j.
Given a set of n control points $\mathbf{X}_i$, where all of the DOF are defined, and a knot vector Ξ, a B-spline curve can be defined as

$$\mathbf{C}(\xi) = \sum_{i=1}^{n} N_i^p(\xi)\mathbf{X}_i.$$

In the same way, multivariate B-spline objects are based on a tensor product of univariate B-splines. Therefore, a B-spline surface can be described with two knot vectors Ξ and $\mathcal{H}$ and a set of $n \cdot m$ control points $\mathbf{X}_{ij}$ such that

$$\mathbf{F}(\xi, \eta) = \sum_{i=1}^{n}\sum_{i=1}^{m} N_i^p(\xi)M_j^q(\eta)\mathbf{X}_{ij} = \sum_{A=1}^{n\cdot m} N_A(\xi, \eta)\mathbf{X}_A.$$

Rational B-splines such as NURBS functions are increasingly used in CAD software since they are capable of exactly representing conic sections. They are not only characterized by control points but also by positive scalar weights w_A and are defined as follows

$$R_A(\xi, \eta) = \frac{N_A(\xi, \eta)w_A}{\sum_{A=1}^{n\cdot m} N_A(\xi, \eta)w_A} = \frac{N_A(\xi, \eta)w_A}{W(\xi, \eta)}.$$

A NURBS surface is now given by

$$\mathbf{F}(\xi, \eta) = \frac{\sum_{A=1}^{n\cdot m} N_A(\xi, \eta)w_A\mathbf{X}_A}{W(\xi, \eta)} = \sum_{A=1}^{n\cdot m} R_A(\xi, \eta)\mathbf{X}_A.$$

3. Reissner-Mindlin plates and shells

3.1. Kinematics

We consider a shell occupying a volume V with mid-surface Ω and thickness t. Let $\mathbf{x}_q$ be the position vector of a material point q of the shell in the physical space and $\boldsymbol{\xi}_q = (\xi, \eta, \zeta)^T$ its counterpart in the parameter space. The coordinate ξ (resp. η) is associated a knot vector Ξ (resp. $\mathcal{H}$) and $\zeta \in [-1, 1]$ defines the transverse position of the point in the parameter space. In other words, the point p corresponding to $\boldsymbol{\xi}_p = (\xi, \eta, 0)^T$ in the parameter space will belong to the mid-surface Ω. Locally, namely on a given patch, the shell volume is the image of the parameter space by the map

$$\mathbf{x}_q(\boldsymbol{\xi}_q) = \mathbf{x}_p(\boldsymbol{\xi}_p) + z\mathbf{n}(\boldsymbol{\xi}_p) = \sum_{A=1}^{n\cdot m} R_A(\xi, \eta)\mathbf{X}_A + \frac{t}{2}\zeta\mathbf{n}(\xi, \eta)$$

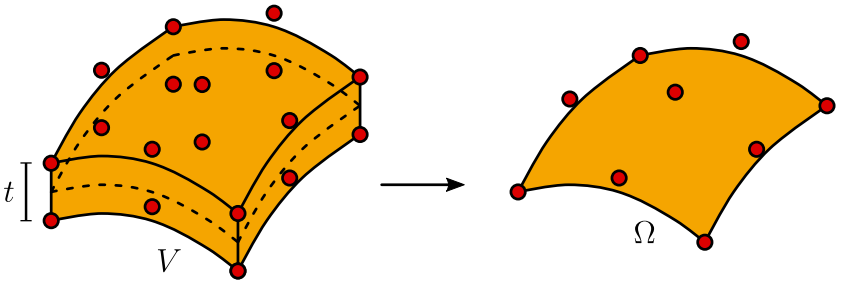

Figure 1: Reissner-Mindlin shell obtained from a degenerated three-dimensional model.

with $\mathbf{n}(\xi,\eta)$ the normal vector to the shell mid-surface at point $\mathbf{x}_p(\xi,\eta)$. The displacement field inside the shell is decomposed locally into a displacement $\mathbf{u}_p(\mathbf{x}_p)$ of the mid-surface and into a rotation of angle $\boldsymbol{\theta}(\mathbf{x}_p)$ of its normal

$$\mathbf{u}_q(\boldsymbol{\xi}_q) = \mathbf{u}_p(\mathbf{x}_p) + z\boldsymbol{\theta}\times\mathbf{n}(\mathbf{x}_p). \tag{1}$$

The expression (1) is obtained supposing small normal rotations in such a way that $(\mathbf{R}(\boldsymbol{\theta})-\mathbf{I}_3)\mathbf{n} \simeq \boldsymbol{\theta}\times\mathbf{n}$ with $\mathbf{R}$ the usual rotation matrix. Extension to large rotations involve a non-linear parametrization $\mathbf{R}(\boldsymbol{\theta})$ of the set of spatial rotations.

3.2. Weak formulation for the shell problem

We wish to take into account transverse shear. Such shell models can be derived from a three-dimensional (3D) one by assuming as done in (1) that the kinematics is linear along the transverse direction, to be possibly characterized by two control points across the thickness, see Figure 1. A plane stress state is also supposed such that $\sigma_{33}=0$ in the element local basis. The actual model, presented in [19], follows the work of Benson et al. [20, 21].

The variational formulation of this shell model was studied in depth in [22], in which it is mentioned as the *basic shell model*. We herein take the same notation to present the corresponding variational formulation. In the following, greek letters will refer to mid-surface quantities with $(\alpha,\beta,\lambda,\mu)\in\{1,2\}$ whereas latin letters will refer to quantities in the volume with $(i,j,k,l)\in\{1,2,3\}$. A subscript is used for quantities expressed in the covariant basis and a superscript for those in the contravariant one. The mid-surface covariant basis $\mathbf{a}_\alpha$ corresponds to the local derivatives $\mathbf{x}_{,\xi}$ or $\mathbf{x}_{,\eta}$ of the in-plane position. Noting $\mathbf{g}_\alpha = \mathbf{a}_\alpha + z\mathbf{a}_{3,\alpha}$ and $\mathbf{g}_3 = \mathbf{a}_3 = \mathbf{n}$, the 3D covariant vectors, the local covariant coordinates of the metric tensor are $g_{\alpha\beta} = \mathbf{g}_\alpha\cdot\mathbf{g}_\beta$ with inverse $g^{\alpha\beta}$.

For a linear analysis, we write the covariant components of the strain tensor for the general displacement (1) as

$$\varepsilon_{ij} = \frac{1}{2}\left(\mathbf{g}_i\cdot\mathbf{u}_{q,j} + \mathbf{g}_j\cdot\mathbf{u}_{q,i}\right).$$

For a linear elastic material, the classical Hooke's law written in the local basis is

$$\sigma^{ij} = C^{ijkl}\varepsilon_{kl},$$

with $\mathbf{C}$ the elastic stiffness tensor defined from Young's modulus E and Poisson's ratio ν. A plane stress state assumption allows us to eliminate the transverse deformation ε_{33} and to simplify the previous equation into

$$\begin{cases}\sigma^{\alpha\beta} = H^{\alpha\beta\lambda\mu}\varepsilon_{\lambda\mu},\\ \sigma^{\alpha 3} = \dfrac{1}{2}G^{\alpha\lambda}\varepsilon_{\lambda 3},\end{cases}\quad\text{with}\quad\begin{cases}H^{\alpha\beta\lambda\mu} = \dfrac{E}{2(1+\nu)}(g^{\alpha\lambda}g^{\beta\mu}+g^{\alpha\mu}g^{\beta\lambda}+\dfrac{2\nu}{1-\nu}g^{\alpha\beta}g^{\lambda\mu}),\\ G^{\alpha\lambda} = \dfrac{2E}{1+\nu}g^{\alpha\lambda}.\end{cases} \tag{2}$$

Using the elastic constitutive relation (2), the action of the stress field associated to the displacement $\mathbf{u}$ in the strain field associated to the virtual displacement $\mathbf{v}$ takes the form

$$\int_{\mathrm{Vol}}\boldsymbol{\sigma}(\mathbf{u}) : \boldsymbol{\epsilon}(\mathbf{v})\mathrm{dVol} = \int_{\mathrm{Vol}}\left(H^{\alpha\beta\lambda\mu}\varepsilon_{\lambda\mu}(\mathbf{u})\varepsilon_{\alpha\beta}(\mathbf{v}) + G^{\alpha\beta}\varepsilon_{\alpha 3}(\mathbf{u})\varepsilon_{\beta 3}(\mathbf{v})\right)\mathrm{dVol}.$$

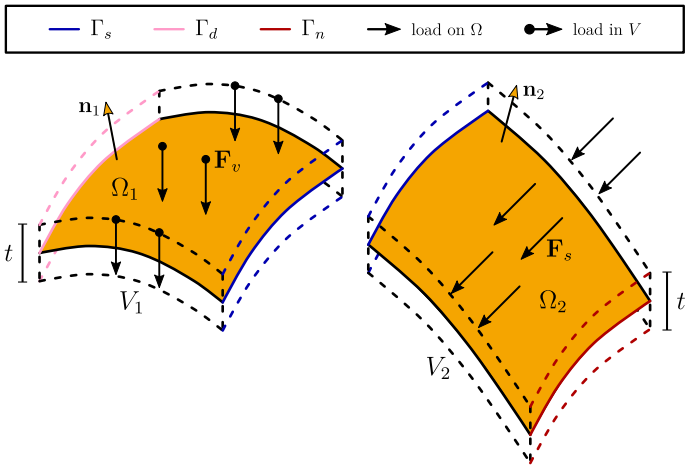

Figure 2: Example of a multipatch shell problem with two domains to glue along the mid interface Γ_s.

The shell mid surface Ω is supposed to be fixed on the part Γ_d^u of its boundary, and no normal rotation is allowed on a possibly different part Γ_d^θ. We then define the Sobolev space $H_d^1(\Omega)$ of admissible test functions by

$$H_d^1(\Omega) = \left\{ \mathbf{v} = (\mathbf{v}_p, \boldsymbol{\vartheta}) \in H^1(\Omega) \times H^1(\Omega), \mathbf{v}_p = \mathbf{0} \text{ on } \Gamma_d^u,\ \boldsymbol{\vartheta} = \mathbf{0} \text{ on } \Gamma_d^\theta \right\}.$$

Then, the Reissner-Mindlin elastic shell problem submitted to an external load reduces to the variational equation

$$\int_{\text{Vol}} \boldsymbol{\sigma}(\mathbf{u}) : \epsilon(\mathbf{v}) \text{dVol} = \int_V \mathbf{f}_v \cdot \mathbf{v}\, dV + \int_\Omega \mathbf{f}_s \cdot \mathbf{v}\, d\Omega + \int_{\partial\Omega} \left(\mathbf{v}_p \cdot \mathbf{g}_p + \boldsymbol{\vartheta} \cdot \mathbf{m}_p \right) d\Gamma, \tag{3}$$

with unknown displacement field $\mathbf{u} \in H_d^1(\Omega)$ and arbitrary test functions $\mathbf{v} \in H_d^1(\Omega)$. Above $\mathbf{f}_v$ and $\mathbf{f}_s$ respectively denote the imposed volumic and surface forces which are applied respectively on V and Ω and $\mathbf{g}_p$ and $\mathbf{m}_p$ are the lateral tension and moment applied on Γ which have to be specified repectively on the complementary parts of Γ_d^u and Γ_d^θ in $\partial\Omega$. The proof of continuity and coercivity of the bilinear form corresponding to the left-hand side of (3) can be found in [22], from which one can deduce existence and uniqueness of the solution of (3).

Remark 1. It can be shown that the coercivity constant has terms in $\mathcal{O}(t)$ for shear and membrane strain components (those who do not vary across the thickness) and in $\mathcal{O}(t^3)$ for bending strain components (those who vary linearly in z). This difference of order in thickness is leading to potential numerical locking that we will address later by using an adequate reduced integration rule. ■

4. Description of a multipatch problem

4.1. Definition of the global domain

We aim at finding displacements of a shell made of different patches with different parametrizations. Let us consider an example with two domains (Figure 2). The two patches, defined from their mid-surfaces Ω_1 and Ω_2, have a common boundary Γ_s. The other boundaries Γ_d and Γ_n correspond to Dirichlet and Neumann boundary conditions, respectively. Edges $\partial\Omega_k$, with $k = \{1, 2\}$, are at least piecewise C^1 such that the outward normal $\boldsymbol{\nu}_k$ for each patch can be uniquely defined almost everywhere.

More generally, let $\Omega \subset \mathbb{R}^3$ be a bounded surface divided into K non-overlapping patches Ω_k which constitute a partition of Ω in such a way that

$$\overline{\Omega} = \bigcup_{k=1}^{K} \overline{\Omega}_k \quad \text{and} \quad \Omega_{k_1} \cap \Omega_{k_2} = \emptyset \text{ with } k_1 \neq k_2.$$

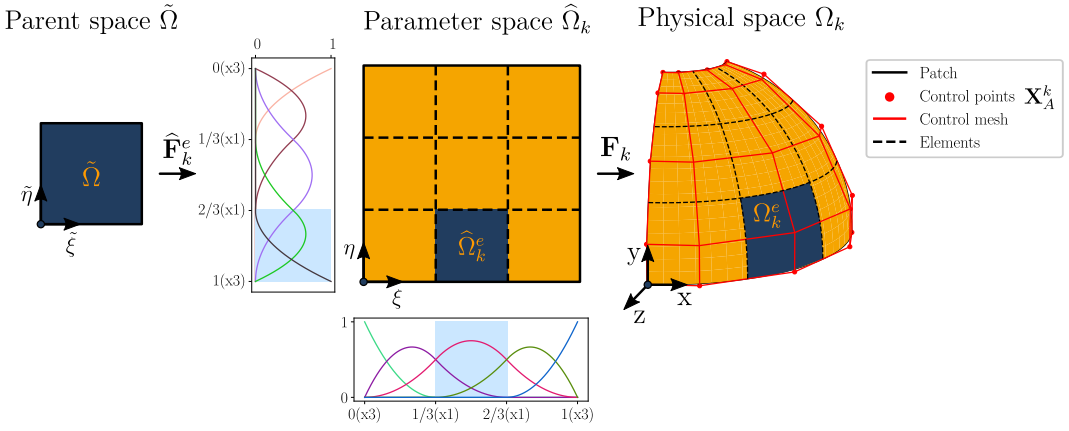

Figure 3: Spaces in IGA and quadratic shape functions for the element $\widehat{\Omega}_k^e$. The center figure describes the mesh and the different elements in the parameter space $\hat{\Omega}_k$ defining the patch k. The figure on the right represents the physical image of the elements and of the associated control points by the mapping $\mathbf{F}_k$ in the case of quadratic B-splines.

We define the NURBS surface of patch Ω_k by

$$\mathbf{F}_k(\xi,\eta) = \sum_{A=1}^{n\cdot m} R_A(\xi,\eta)\,\mathbf{X}_A^k,$$

recalling that $\mathbf{X}_A \in \mathbb{R}^3$ are the control points coordinates. We denote by $\mathcal{M}_k$ the mesh in the physical space, which is the image of $\widehat{\mathcal{M}}_k$ in the parameter space by $\mathbf{F}_k$. Let $\mathbf{O}$ and $\mathbf{Q}$ be elements respectively in the physical and parameter space (Figure 3). Consequently, we can write

$$\mathcal{M}_k = \left\{ \mathbf{O} \subset \Omega_k \,:\, \mathbf{O} = \mathbf{F}_k(\mathbf{Q}), \mathbf{Q} \in \widehat{\mathcal{M}}_k \right\}.$$

An interface γ_{kl} is defined as the closure of the intersection between two domain boundaries

$$\gamma_{kl} = \overline{\partial\Omega_k \cap \partial\Omega_l} \quad \text{with} \quad 1 \le l < k \le K.$$

All of theses interfaces are defining the skeleton $\Gamma_s = \bigcup_{k>l} \gamma_{kl}$. The master-slave approach is retained in order to define a hierarchy between domains constituting an interface. The slave side $s(kl) \in \{k, l\}$, is a priori arbitrary . We can point out that a patch can be defined as a slave for an interface and as a master for another one.

With the previous notation, each interface γ_{kl} is defined from the intersection of a slave side $\overline{\partial\Omega_{s(kl)}}$ and a master one $\overline{\partial\Omega_{m(kl)}}$. Knowing that, we distinguish three types of geometrical conformities. A geometrical conforming situation is when γ_{kl} is an entire edge on both sides $\gamma_{kl} = \overline{\partial\Omega_{s(kl)}} = \overline{\partial\Omega_{m(kl)}}$, Figure 4 (a). A slave conforming case, as detailed in [18], corresponds to a situation where γ_{kl} is an entire edge of the slave side $\Omega_{s(kl)} = \mathbf{F}_{s(kl)}(\widehat{\Omega}_{s(kl)})$, i.e., $\gamma_{kl} = \overline{\partial\Omega_{s(kl)}}$ as shown in Figure 4 (b). All of the other situations are presented in Figure 4 (c).

4.2. Weak formulation for the multipatch problem

We begin by setting the abstract framework as introduced in [18, 23]. The initial weak formulation (3) is set on $H_d^1(\Omega)$. We split it into local spaces

$$V_k(\Omega_k) = H_d^1(\Omega_k) = \left\{ \mathbf{v}_k = ((\mathbf{v}_p)_k, \vartheta_k) \in H^1(\Omega_k) \times H^1(\Omega_k),\ (\mathbf{v}_p)_k\big|_{\Gamma_d^u} = \mathbf{0},\ \ \vartheta_k|_{\Gamma_d^\theta} = \mathbf{0} \right\}$$

and define the local bilinear and linear forms a_k and L_k by

$$a_k(\mathbf{u}_k, \mathbf{v}_k) = \int_{\mathrm{Vol}_k} \boldsymbol{\sigma}(\mathbf{u}_k) : \boldsymbol{\epsilon}(\mathbf{v}_k)\mathrm{dVol}_k,$$

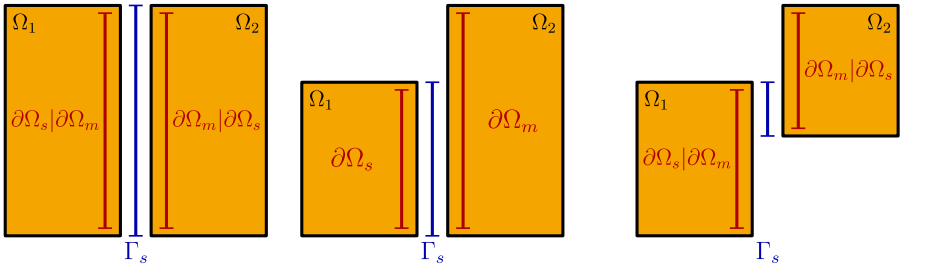

(a) $\gamma_{kl} = \overline{\partial\Omega_{s(kl)}} = \overline{\partial\Omega_{m(kl)}}$ (b) $\gamma_{kl} = \overline{\partial\Omega_{s(kl)}}$ (c) $\gamma_{kl} = \overline{\partial\Omega_{s(kl)} \cap \partial\Omega_{m(kl)}} \neq \overline{\partial\Omega_{s(kl)}}$

Figure 4: Three different cases of patch interface geometry: geometrical conforming (a), slave conforming (b) and totally non-conforming (c).

$$L_k(\mathbf{v}_k) = \int_{\mathrm{Vol}_k} (\mathbf{f}_v)_k \cdot \mathbf{v}_k \mathrm{dVol}_k + \int_{\Omega_k} (\mathbf{f}_s)_k \cdot \mathbf{v}_k \mathrm{d}\Omega_k + \int_{\Gamma_n \cap \bar{\Omega}_k} (\mathbf{v}_p)_k \cdot (\mathbf{g}_p)_k + \boldsymbol{\vartheta}_k \cdot (\mathbf{m}_p)_k \mathrm{d}\Gamma_n,$$

with Vol_k the volume of the shell associated with the mid-surface Ω_k.

We are now interested in the coupling term that will link each patch of Ω. In order to give a functional framework, we define the broken Sobolev space $V = \prod_k V_k$ associated with the broken norm

$$||\mathbf{v}||_V^2 = \sum_k ||\left(\mathbf{v}_p\right)_k||_{H^1(\Omega_k)}^2 + ||\boldsymbol{\vartheta}_k||_{H^1(\Omega_k)}^2.$$

By a standard integration by part, we classically prove that

$$H_d^1(\Omega) = \left\{ \{\mathbf{v}_k\} \in V,\ \left\{\mathrm{Tr}_{kl}\mathbf{v}_k - \mathrm{Tr}_{kl}\mathbf{v}_l\right\}_{\gamma_{kl}} = \mathbf{0},\ \forall kl \right\}, \tag{4}$$

with $\mathrm{Tr}_{kl}\mathbf{v}_m$ the trace of $\mathbf{v}_m$ on γ_{kl} . Inside this space we have $a(\mathbf{u}, \mathbf{v}) = \sum_k a_k(\mathbf{u}_k, \mathbf{v}_k)$, with $\mathbf{v}_k$ the standard restriction of $\mathbf{v}$ on Ω_k, expression to be used in the variational problem (3).

4.3. Local discretization

We recall that each patch is defined by the NURBS parametrization $\mathbf{F}_k$ which needed two knots vectors $\boldsymbol{\Xi}_k = \left\{\Xi_k, \mathcal{H}_k\right\}$ such that the physical space Ω_k is the image of $\widehat{\Omega}_k$ by $\mathbf{F}_k$ (Figure 3). We use the same shape functions R_A to represent the admissible displacements of the shell,

$$\mathbf{u}_q(\xi_q) = \mathbf{u}_p(\mathbf{x}_p) + z\boldsymbol{\theta} \times \mathbf{n}(\mathbf{x}_p) = \sum_{A=1}^{n \cdot m} R_A(\xi, \eta) \left(\mathbf{U}_A + \frac{t}{2}\zeta\boldsymbol{\theta}_A \times \mathbf{n}(\xi, \eta)\right), \tag{5}$$

with $\mathbf{U}_A$ (resp. $\boldsymbol{\theta}_A$) the displacements (resp. rotations) vector at control point of coordinates $\mathbf{X}_A$. Consequently, we can define the discrete space of displacements $V_{k,h} \subset V_k$ by

$$V_{k,h} = \left\{\mathbf{v}_k = \widehat{\mathbf{v}}_k \circ \mathbf{F}_k^{-1},\ \widehat{\mathbf{v}}_k \in R^{\mathbf{p}_k}(\boldsymbol{\Xi}_k)^2\right\},$$

with $R^{\mathbf{p}_k}(\boldsymbol{\Xi}_k) = R^{p_k}(\Xi_k) \otimes R^{p_k}(\mathcal{H}_k)$ the space generated by tensorial product of the space of NURBS functions of order p_k defined on Ξ_k and $\mathcal{H}_k$ respectively.

We also introduce a finite dimensional approximation $M_{kl,h} = M_{lk,h}$ of the space of interface forces acting on $\gamma_{kl} = \gamma_{lk}$

$$M_{kl,h} \subset L^2(\gamma_{kl})^2.$$

In order to apply the continuity constraint at a discrete level, we define the continuous bilinear form c_{kl} by

$$c_{kl} : L^2(\gamma_{kl})^2 \times L^2(\gamma_{kl})^2 \to \mathbb{R}, \quad (\lambda_{kl}, \mathbf{u}_{kl}) \mapsto \int_{\gamma_{kl}} \lambda_{kl} \cdot \mathbf{u}_{kl}\, \mathrm{d}\gamma_{kl}, \tag{6}$$

and approximate the displacement space (4) by the kernel

$$\mathrm{Ker}(\mathbf{C}_h) = \left\{ \mathbf{v}_k = \left((\mathbf{v}_p)_k, \boldsymbol{\vartheta}_k\right) \in V_h = \prod_k V_{k,h},\ c_{kl}\left(\boldsymbol{\mu}_{kl}, \mathrm{Tr}_{kl}\mathbf{v}_k - \mathrm{Tr}_{kl}\mathbf{v}_l\right) = 0, \forall \boldsymbol{\mu}_{kl} \in M_{kl,h}, \forall kl \right\}.$$

4.4. Dualised discrete problem

With the previous notation, the discrete abstract problem consists in finding $\left\{\mathbf{u}_k\right\} \in \mathrm{Ker}(\mathbf{C}_h)$ such that we have

$$\sum_k a_k(\mathbf{u}_k, \mathbf{v}_k) = \sum_k L_k(\mathbf{v}_k), \forall \left\{\mathbf{v}_k\right\} \in \mathrm{Ker}(\mathbf{C}_h). \tag{7}$$

We can remark that $\mathrm{Ker}(\mathbf{C}_h)$ is the kernel of the linear application $\mathbf{C}_h : \prod_k V_{k,h} \to \left(\prod_{k>l} M_{kl,h}\right)'$ defined by (6). It will be handled by Lagrange multipliers [24, 25] as already applied for plane elasticity in the context of IGA in [11, 18]. From the closed range theorem applied in a finite dimensional setting, $\mathrm{Im}(\mathbf{C}_h^T) = \mathrm{Ker}(\mathbf{C}_h)^\perp$ and thus there exists a multiplier field $\boldsymbol{\lambda} = \{\boldsymbol{\lambda}_{kl}\} = \{(\lambda^u_{kl}, \lambda^\theta_{kl})\} \in \left(\prod_{k>l} M_{kl,h}\right)$ such that (7) can be rewritten as finding $\left\{\mathbf{u}_k\right\} \in V_h = \prod_k V_{k,h}$ and $\left\{\boldsymbol{\lambda}_{kl}\right\} \in M_h = \prod_{k>l} M_{kl,h}$ such that

$$\begin{aligned} \sum_k a_k(\mathbf{u}_k, \mathbf{v}_k) + \sum_{k>l} c_{kl}\left(\boldsymbol{\lambda}_{kl}, \mathrm{Tr}_{kl}\mathbf{v}_k - \mathrm{Tr}_{kl}\mathbf{v}_l\right) &= \sum_k L_k(\mathbf{v}_k), \qquad \forall \left\{\mathbf{v}_k\right\} \in V_h, \\ \sum_{k>l} c_{kl}\left(\boldsymbol{\mu}_{kl}, \mathrm{Tr}_{kl}\mathbf{u}_k - \mathrm{Tr}_{kl}\mathbf{u}_l\right) &= 0, \qquad \forall \left\{\boldsymbol{\mu}_{kl}\right\} \in M_h. \end{aligned} \tag{8}$$

When we have non-conforming meshes at an interface, this formulation is often called mortar method [26]. The dualised formulation (8) is a saddle-point problem. The coercivity of the corresponding bilinear form is no longer insured. Consequently, the choice of a suitable dual space is essential to preserve the uniqueness of the solution [18, 23, 27]. Classical mortar theory requires the satisfaction of two main assumptions to be detailed later. The first one is the classical inf-sup condition, often called L.B.B. (Ladyženskaja-Babuška-Brezzi [28, 29]) whereas the second one corresponds to the approximation order for the chosen dual space.

4.5. Augmented discrete problem

An augmented lagrangian formulation, sometimes called hybrid or mixed method, introduces an additional primal term in (8) which locally reinforces the continuity constraint, see [30, 31], yielding additional robustness both from an approximation and an algorithmic point of view. This method is a combination of a penalty approach [32, 33] and of the previous dualised problem. The penalty term uses the following continuous bilinear form

$$b_{kl} : \prod_k V_k \times \prod_k V_k \to \mathbb{R}, \quad (\mathbf{u}_k, \mathbf{v}_k) \mapsto \int_{\gamma_{kl}} \left(\mathrm{Tr}_{kl}\mathbf{u}_k - \mathrm{Tr}_{kl}\mathbf{u}_l, \mathrm{Tr}_{kl}\mathbf{v}_k - \mathrm{Tr}_{kl}\mathbf{v}_l\right) \mathrm{d}\gamma_{kl}.$$

Noting by α_{kl} the penalty factor associated to the interface γ_{kl}, we are now able to write the penalised dualised discrete problem as finding $\left\{\mathbf{u}_k\right\} \in V_h = \prod_k V_{k,h}$ and $\left\{\boldsymbol{\lambda}_{kl}\right\} \in M_h = \prod_{k>l} M_{kl,h}$ such that

$$\begin{aligned} \sum_k a_k(\mathbf{u}_k, \mathbf{v}_k) + \sum_{k>l} \alpha_{kl}\, b_{kl}(\mathbf{u}_k, \mathbf{v}_k) + \sum_{k>l} c_{kl}\left(\boldsymbol{\lambda}_{kl}, \mathrm{Tr}_{kl}\mathbf{v}_k - \mathrm{Tr}_{kl}\mathbf{v}_l\right) &= \sum_k L_k(\mathbf{v}_k), \qquad \forall \left\{\mathbf{v}_k\right\} \in V_h, \\ \sum_{k>l} c_{kl}\left(\boldsymbol{\mu}_{kl}, \mathrm{Tr}_{kl}\mathbf{u}_k - \mathrm{Tr}_{kl}\mathbf{u}_l\right) &= 0, \qquad \forall \left\{\boldsymbol{\mu}_{kl}\right\} \in M_h. \end{aligned}$$

For this augmented form, the choice of the penalty factor is not as essential as in a pure penalty method written without Lagrange multipliers.

5. Convergence analysis

5.1. Geometric assumptions

For the analysis to come, we make the same assumptions as [18] for the regularity of the physical mapping $\mathbf{F}_k$. We will consider that we have the same order p_k for the shape functions in the two parametric directions and assume that

Assumption 1 (Physical mapping $\mathbf{F}_k$). The mapping $\mathbf{F}_k$ on each patch k is regular, with its inverse $\mathbf{F}_k^{-1}$ well-defined, and piecewise differentiable at any order with bounded derivatives. ■

With the notation $h_{\mathbf{Q}} = \text{diam}(\mathbf{Q})$ and $h_{\mathbf{O}} = \text{diam}(\mathbf{O})$ standing for, respectively, the characteristic length of the mesh in the parameter and physical space, Assumption 1 claims that on each patch $h_{\mathbf{Q}} \simeq h_{\mathbf{O}}$. We denote by h_k the characteristic mesh size on the patch

$$h_k = \max\left\{h_{\mathbf{Q}}, \mathbf{Q} \in \widehat{\mathcal{M}}_k\right\} \simeq \max\left\{h_{\mathbf{O}}, \mathbf{O} \in \mathcal{M}_k\right\}.$$

We further restrict our analysis to quasi-uniform meshes.

Assumption 2 (Globally quasi-uniform mesh, Assumption 2 in [18]). We consider the partition formed from the breakpoints of $\Xi = \left\{\xi_1, \dots, \xi_{n+p+1}\right\}$ and $\mathcal{H} = \left\{\eta_1, \dots, \eta_{m+p+1}\right\}$. Then there exists a constant $C_{\theta,k} \geq 1$ such that all elements $h_i^1 = \xi_{i+1}^* - \xi_i^*$ and $h_j^2 = \eta_{j+1}^* - \eta_j^*$ in the patch satisfy

$$C_{\theta,k}^{-1} \leq \frac{h_i^\delta}{h_j^{\delta'}} \leq C_{\theta,k},\ \forall i, \forall j, \forall(\delta, \delta') \in \{1,2\}. \quad ■$$

The simplifying Assumption 2, which forbids graded meshes, considers the characteristic size h_k to be quasi-uniform along elements and along the two parametric directions ξ and η. Under Assumption 2, which involves a globally quasi-uniform mesh, it is well-known that NURBS have optimal approximation properties as proved in [34].

Lemma 1 (NURBS optimal approximation)**.** *We consider a quasi-uniform mesh and integers r and s such that $0 \leq r \leq s \leq p_k + 1$. We denote by C_{shape} a constant depending on p_k, $C_{\theta,k}$, $\mathbf{F}_k$ and on the weights w_A used to construct the NURBS functions. Then, $\forall \mathbf{v}_k = ((\mathbf{v}_p)_k, \boldsymbol{\vartheta}_k) \in H^s(\Omega_k)^2$, there exists a locally defined approximation $\mathbf{v}_{k,h} \in V_{k,h}$ such that*

$$||\mathbf{v}_k - \mathbf{v}_{k,h}||_{H^r(\Omega_k)^2} \leq C_{shape} h_k^{s-r} ||\mathbf{v}_k||_{H^s(\Omega_k)^2},$$

with $||\mathbf{v}_k||^2_{H^s(\Omega_k)^2} = ||(\mathbf{v}_p)_k||^2_{H^s(\Omega_k)} + ||\boldsymbol{\vartheta}_k||^2_{H^s(\Omega_k)}$. □

5.2. Assumptions on the dual space

The purpose of this section is to briefly review the convergence analysis which justifies specific choices of mortar spaces, and possibly adapt it to our multipatch isogeometric thick shell framework. Convergence results on the mortar method have been presented in [23, 26, 35–38]. This approximation strategy is non-conforming and thus, the error in the discrete solution (8) is to be decomposed into an approximation error and a consistency error. A technical difficulty arises because traces of solutions on adjacent interfaces are not independent from one face to another, while our discretisation strategy splits the continuity constraint in independent local weak continuity conditions. To overcome this difficulty, one introduces the reduced space $W_{kl,h}$ of traces of the slave space $V_{s(kl),h}$ on γ_{kl} having zero values at interface ends

$$W_{kl,h} = \text{Tr}_{kl} V_{s(kl),h} \cap H^{1/2}_{0,0}(\gamma_{kl})^2$$

on which to check the local inf-sup condition [39], [18, Assumption 4]. In this framework, the multipatch isogeometric analysis of shell introduces two additional technicalities : the complexity of the underlying variational form with rotational degrees of freedom, and the non interpolatory character of the NURBS shape function at cross points. This last difficulty was already faced by [18] and imposes to use weighted L^2 norms on the interfaces as in [36].

Denoting by C a constant independent of the mesh size, but possibly dependent on the approximation order p_k, we introduce our three main assumptions to be checked later for specific choices of trace spaces. The first one is the standard inf-sup stability condition

Assumption 3 (Local Inf-sup stability). For any $l < k \in \{1, \dots, K\}$ and $\forall \boldsymbol{\mu}_{kl} \in M_{kl,h}$ we have

$$\sup_{\mathbf{w}_k \in W_{kl,h}} \frac{\int_{\gamma_{kl}} \mathbf{w}_k \boldsymbol{\mu}_{kl} \, \mathrm{d}\gamma_{kl}}{||\mathbf{w}_k||_{L^2(\gamma_{kl})^2}} \geq C ||\boldsymbol{\mu}_{kl}||_{L^2(\gamma_{kl})^2}. \quad ■$$

This condition ensures the L^2 continuity of the $M_{kl,h}$ orthogonal projection operator $\mathbf{\Pi}_{kl,h}$ onto $W_{kl,h}$ defined as the closest point $\mathbf{\Pi}_{kl,h}(\mathbf{v}) \in W_{kl,h}$ such that

$$\int_{\gamma_{kl}} \boldsymbol{\mu}_{kl,h} \mathbf{\Pi}_{kl,h}(\mathbf{v}) \, \mathrm{d}\gamma_{kl} = \int_{\gamma_{kl}} \boldsymbol{\mu}_{kl,h} \mathbf{v} \, \mathrm{d}\gamma_{kl}, \forall \boldsymbol{\mu}_{kl,h} \in M_{kl,h}, \mathbf{\Pi}_{kl,h}(\mathbf{v}) \in W_{kl,h}.$$

Lemma 2 (L^2 stability of interface projection [36])**.** *Under Assumption 3, we have*

$$||\mathbf{\Pi}_{kl,h}(\mathbf{v})||_{L^2(\gamma_{kl})^2} \leq \frac{1}{C} ||\mathbf{v}||_{L^2(\gamma_{kl})^2}, \forall \mathbf{v} \in L^2(\gamma_{kl})^2.$$ □

The next assumption ensures that interface forces can be optimally approximated by our space of interface Lagrange multipliers [18, Assumption 5].

Assumption 4 (Optimal interface approximation). For any $l < k \in \{1, \dots, K\}$, there exists an approximation order $\eta(kl)$ such that $\forall \boldsymbol{\lambda} = (\boldsymbol{\lambda}^u, \boldsymbol{\lambda}^\theta) \in H^{\eta(kl)}(\gamma_{kl})^2$ we have

$$\inf_{\boldsymbol{\mu}_{kl} \in M_{kl,h}} ||\boldsymbol{\lambda} - \boldsymbol{\mu}_{kl}||_{L^2(\gamma_{kl})^2} \leq C h_{kl}^{\eta(kl)} ||\boldsymbol{\lambda}||_{H^{\eta(kl)}(\gamma_{kl})^2},$$

with $||\boldsymbol{\lambda}||^2_{H^{\eta(kl)}(\gamma_{kl})^2} = ||\boldsymbol{\lambda}^u||^2_{H^{\eta(kl)}(\gamma_{kl})} + ||\boldsymbol{\lambda}^\theta||^2_{H^{\eta(kl)}(\gamma_{kl})}$. ■

The last assumption guarantees that the weak continuity condition implies strong continuity of the rigid body motions. It is satisfied for example as soon as $M_{kl,h}$ contains linear functions or smooth positive bubble functions.

Assumption 5 (Coarse dual space for rigid body motions). For any interface γ_{kl}, $l < k \in \{1, \dots, K\}$, there exists a small subset $M_{kl,0} \subset M_{kl,h}$ independent of h_k such that if $\mathbf{v}_k$ and $\mathbf{v}_l$ are rigid body motions respectively on Ω_k and Ω_l satisfying

$$\int_{\gamma_{kl}} \boldsymbol{\mu}_{kl} (\mathbf{v}_k - \mathbf{v}_l) \, \mathrm{d}\gamma_{kl} = 0, \ \forall \boldsymbol{\mu}_{kl} \in M_{kl,0},$$

then $\mathbf{v}_k = \mathbf{v}_l$ on γ_{kl}. ■

5.3. Convergence results

5.3.1. Equivalence of norms

Our goal here is to prove the equivalence between the energy norm and the broken H^1 norm on

$$\mathrm{Ker}(\mathbf{C}_0) = \left\{ \mathbf{v}_k = \left((\mathbf{v}_p)_k, \boldsymbol{\vartheta}_k \right) \in V, \, c_{kl} \left(\boldsymbol{\mu}_{kl}, \mathrm{Tr}_{kl} \mathbf{v}_k - \mathrm{Tr}_{kl} \mathbf{v}_l \right) = 0, \forall \boldsymbol{\mu}_{kl} \in M_{kl,0}, \forall kl \right\}.$$

Proposition 3. *Under Assumption 5 and if the global boundary conditions are such that there are no non zero global rigid body motions in $H^1_d(\Omega)$, the energy norm is equivalent to the H^1 broken norm on* $\mathrm{Ker}(\mathbf{C}_0)$

$$a(\mathbf{v}, \mathbf{v}) = \sum_k a_k(\mathbf{v}_k, \mathbf{v}_k) \simeq ||\mathbf{v}||^2_V = \sum_k ||\mathbf{v}_k||^2_{H^1(\Omega_k)^2}, \forall \mathbf{v} \in \mathrm{Ker}(\mathbf{C}^0),$$

the constant of equivalence being thickness dependent. □

Proof. The proof adapts the proof by contradiction of [22]. We give it for completeness since it illustrates the role of the coarse dual space. If the equivalence did not hold, there would exist a sequence $(\mathbf{v}^n)$ in $\mathrm{Ker}(\mathbf{C}^0)$ such that

$$\begin{cases} \sum_k a_k(\mathbf{v}^n_k, \mathbf{v}^n_k) \underset{n \to \infty}{\to} 0, \\ \sum_k ||\mathbf{v}^n_k||^2_{H^1(\Omega_k)^2} = 1. \end{cases}$$

From the second condition, there would exist a subsequence still denoted $(\mathbf{v}_k^n)$ weakly converging in $H^1(\Omega_k)^2$ and hence strongly converging in $L^2(\Omega_k)^2$. From the convergence towards zero in energy norm and the local H^1 ellipticity

$$a_k(\mathbf{v}_k, \mathbf{v}_k) + ||\mathbf{v}_k||^2_{L^2(\Omega_k)^2} \geq c\|\mathbf{v}_k\|^2_{H^1(\Omega_k)^2}$$

proved in [22], Proposition 4.3.2, the subsequence is also a Cauchy sequence for the broken H^1 norm. Hence, this subsequence $(\mathbf{v}_k^n)$ converge to $\mathbf{v}^\infty$ in $\mathrm{Ker}(\mathbf{C}^0)$ and by construction, we have

$$\begin{cases} \sum_k a_k(\mathbf{v}^\infty, \mathbf{v}^\infty) = 0, \\ \sum_k ||\mathbf{v}_k^\infty||^2_{H^1(\Omega_k)^2} = 1. \end{cases}$$

The limit $\mathbf{v}^\infty$ is therefore a local rigid motion, which is continuous at the interfaces from Assumption 5. It is thus a global rigid motion in $H^1_d(\Omega)$, hence it must be equal to zero, which is in contradiction with above. Observe that this proof does not provide any hint on how the constant of equivalence will vary with respect to the number of subdomains or with their size or shape. ■

5.3.2. Consistency Error

Proposition 4 (Consistency)**.** *Under Assumption 4, any solution* $\mathbf{u}$ *of* (3) *which belongs to* $H^{r+1}(\Omega)^2$ *with* $1/2 < r \leq \min_{kl}(\eta(kl) + 1/2)$ *satisfies*

$$\sup_{\mathbf{v}_h \in \mathrm{Ker}(\mathbf{C}_h)} \frac{|a(\mathbf{u}, \mathbf{v}_h) - L(\mathbf{v}_h)|}{||\mathbf{v}_h||_V} \leq C \sqrt{\sum_k h_k^{2r} ||\mathbf{u}_k||^2_{H^{r+1}(\Omega_k)^2}}.$$ □

Proof. This is an easy extension of [23] adapted to the variational formulation of a thick shell problem. Let $\boldsymbol{\nu}_k$ denote the outgoing normal to the surface contour $\partial\Omega_k$, not to be confused with the shell normal. Let $\boldsymbol{P}$ be the projection onto the mid-surface Ω, $\frac{|\mathrm{d}S|}{|\mathrm{d}a|}$ denote the ratio between the area of an element $\mathrm{d}S$ of the tangent space at distance z from the mid-surface and the area of its projection $\mathrm{d}a$ on the mid-surface, $\boldsymbol{N}$ and $\boldsymbol{M}$ be the generalized tension and moment tensors defined by

$$\boldsymbol{N} = \int_{-t/2}^{t/2} \boldsymbol{P} \cdot \boldsymbol{\sigma} \cdot \boldsymbol{P}^t \, \frac{|\mathrm{d}S|}{|\mathrm{d}a|} \mathrm{d}z, \quad \boldsymbol{M} = \int_{-t/2}^{t/2} z\boldsymbol{P} \cdot \boldsymbol{\sigma} \cdot \boldsymbol{P}^t \, \frac{|\mathrm{d}S|}{|\mathrm{d}a|} \mathrm{d}z$$

and $\mathbf{q}$ and $\mathbf{r}$ denote the first and second order shear force vectors defined by

$$\mathbf{q} = \int_{-t/2}^{t/2} \boldsymbol{\sigma} \cdot \mathbf{n} \frac{|\mathrm{d}S|}{|\mathrm{d}a|} \mathrm{d}z, \quad \mathbf{r} = \int_{-t/2}^{t/2} z\boldsymbol{\sigma} \cdot \mathbf{n} \frac{|\mathrm{d}S|}{|\mathrm{d}a|} \mathrm{d}z.$$

From the plane stress assumptions, these vectors have no components along $\mathbf{g}_3 = \mathbf{n}$. We therefore have

$$\int_{-t/2}^{t/2} \boldsymbol{\sigma} \frac{|\mathrm{d}S|}{|\mathrm{d}a|} \mathrm{d}z = \boldsymbol{N} + \mathbf{n} \otimes \mathbf{q} + \mathbf{q} \otimes \mathbf{n}$$

and

$$\int_{-t/2}^{t/2} z\boldsymbol{\sigma} \cdot \frac{|\mathrm{d}S|}{|\mathrm{d}a|} \mathrm{d}z = \boldsymbol{M} + \mathbf{n} \otimes \mathbf{r} + \mathbf{r} \otimes \mathbf{n}.$$

By construction of the displacement field $(\mathbf{v}_q)_k = ((\mathbf{v}_p)_k + z\boldsymbol{\vartheta}_k \times \mathbf{n})(\mathbf{x}_p)$ whose gradient is

$$\boldsymbol{\nabla}(\mathbf{v}_q)_k = \frac{\partial}{\partial \mathbf{x}_p}((\mathbf{v}_p)_k + z\boldsymbol{\vartheta}_k \times \mathbf{n}) \cdot \boldsymbol{P} + \boldsymbol{\vartheta}_k \times \mathbf{n} \otimes \mathbf{n}$$

the local variational form writes

$$a_k(\mathbf{u}, \mathbf{v}_k) \quad = \quad \int_{\mathrm{Vol}_k} \boldsymbol{\sigma}(\mathbf{u}) : \boldsymbol{\epsilon}(\mathbf{v}_k) \, \mathrm{dVol}_k$$

$$
\begin{aligned}
&= \int_{\Omega_k}\int_{-t/2}^{t/2} \boldsymbol{\sigma} : \boldsymbol{\nabla}(\mathbf{v}_q)_k \frac{|\mathrm{d}S|}{|\mathrm{d}a|}\mathrm{d}z\,\mathrm{d}\Omega_k \\
&= \int_{\Omega_k}\left((\boldsymbol{N}+\mathbf{n}\otimes\mathbf{q}) : \frac{\partial(\mathbf{v}_p)_k}{\partial\mathbf{x}_p} + (\boldsymbol{M}+\mathbf{n}\otimes\mathbf{r}) : \frac{\partial(\boldsymbol{\vartheta}_k\times\mathbf{n})}{\partial\mathbf{x}_p} + \mathbf{q}\cdot(\boldsymbol{\vartheta}_k\times\mathbf{n})\right)\mathrm{d}\Omega_k \\
&= -\int_{\Omega_k}\left(\left(\mathrm{div}_\Omega(\boldsymbol{N}+\mathbf{n}\otimes\mathbf{q}) - \boldsymbol{N} : \frac{\partial\mathbf{n}}{\partial\mathbf{x}_p}\right)\cdot(\mathbf{v}_p)_k + \mathbf{n}\times\left(\mathrm{div}_\Omega(\boldsymbol{M}+\mathbf{n}\otimes\mathbf{r}) - \mathbf{q}\right)\cdot\boldsymbol{\vartheta}_k\right)\mathrm{d}\Omega_k \\
&\quad + \int_{\partial\Omega_k}\left((\boldsymbol{N}\cdot\boldsymbol{\nu}_k + \mathbf{n}\,\mathbf{q}\cdot\boldsymbol{\nu}_k)\cdot(\mathbf{v}_p)_k + (\mathbf{n}\times\boldsymbol{M}\cdot\boldsymbol{\nu}_k)\cdot\boldsymbol{\vartheta}_k\right)\mathrm{d}\partial\Omega_k.
\end{aligned}
$$

The presence of the surface second form $\frac{\partial\mathbf{n}}{\partial\mathbf{x}_p}$ after the divergence in the above expression corresponds to the contribution of the spatial variation of the test function occuring at frozen normal component $(\mathbf{v}_p)_k\cdot\mathbf{n}$.

Since the solution $\mathbf{u}_k \in H^{r+1}(\Omega_k)^2$ satisfies the local equation of equilibrium, the first integral cancels for any test functions $(\mathbf{v}_p, \boldsymbol{\vartheta})$ in $H^1(\Omega_k)\times H^1(\Omega_k)$, and thus we have

$$
a_k(\mathbf{u},\mathbf{v}_h) - L_k(\mathbf{v}_h) = \sum_l \int_{\gamma_{kl}} \boldsymbol{\lambda}_k\cdot\mathbf{v}_{k,h}\mathrm{d}\gamma_{kl}
$$

under the notation $\boldsymbol{\lambda}_k = \{\boldsymbol{N}\cdot\boldsymbol{\nu}_k + \mathbf{n}\,\mathbf{q}\cdot\boldsymbol{\nu}_k, \mathbf{n}\times\boldsymbol{M}\cdot\boldsymbol{\nu}_k\}$. Hence, after summation on the different patches, we get

$$
a(\mathbf{u},\mathbf{v}_h) - L(\mathbf{v}_h) = \sum_{k>l}\int_{\gamma_{kl}} \boldsymbol{\lambda}_k\cdot(\mathbf{v}_{k,h}-\mathbf{v}_{l,h})\mathrm{d}\gamma_{kl}.
$$

By construction of $\mathbf{v}_h = \left\{(\mathbf{v}_p)_h, \boldsymbol{\vartheta}_h\right\} \in \mathrm{Ker}(\mathbf{C}_h)$, their interface jumps are orthogonal to the dual interface spaces, and hence, by introducing successively the L^2 projections $\boldsymbol{\mu}_{kl,h}$ of $\boldsymbol{\lambda}_k$ onto $M_{kl,h}$ and any arbritrary elements $\hat{\boldsymbol{\mu}}_{kl,h}$ in $M_{kl,h}$, we get

$$
a(\mathbf{u},\mathbf{v}_h) - L(\mathbf{v}_h) = \sum_{k>l}\int_{\gamma_{kl}} (\boldsymbol{\lambda}_k - \boldsymbol{\mu}_{kl,h})\cdot(\mathbf{v}_{k,h}-\mathbf{v}_{l,h}-\hat{\boldsymbol{\mu}}_{kl,h})\mathrm{d}\gamma_{kl}
$$

from which we conclude from a direct application of Assumption 4 on each factor inside the integral and the use of the Cauchy Schwarz inequality. ■

5.3.3. Approximation error

Let $\mathbf{I}_h = \left\{\mathbf{I}_{k,h}\right\}$ be the optimal approximation used in Lemma 1. Let $\mathbf{E}_{kl,h} : W_{kl,h} \to V_{s(kl),h}$ be the extension obtained by taking a zero value on each control point of the slave patch which is not on γ_{kl}. Inspired from [23] and using the notation of [40], we introduce the local projector $\mathbf{P}_h$ defined by

$$
\begin{aligned}
\mathbf{P}_h : H^{r+1}(\Omega)^2 &\to \mathrm{Ker}(\mathbf{C}_h), \\
\mathbf{v} &\mapsto \mathbf{I}_h(\mathbf{v}) - \sum_{k>l}\mathbf{E}_{kl,h}\circ\boldsymbol{\Pi}_{kl,h}\left[\mathbf{I}_h(\mathbf{v})\right].
\end{aligned}
$$

The local projection $\boldsymbol{\Pi}_{kl,h}$ enables to move any interface jumps away from the cross points and hence to correct it locally on each interface. Since $\boldsymbol{\Pi}_{kl,h}$ is orthogonal to $M_{kl,h}$, we observe that this projection is indeed in $\mathrm{Ker}(\mathbf{C}_h)$ since we have

$$
\begin{aligned}
\int_{\gamma_{kl}} \boldsymbol{\mu}_{kl,h}\left[\mathbf{P}_h(\mathbf{v})\right]\,\mathrm{d}\gamma_{kl} &= \int_{\gamma_{kl}} \boldsymbol{\mu}_{kl,h}\left[\mathbf{I}_h(\mathbf{v})\right] - \boldsymbol{\mu}_{kl,h}\boldsymbol{\Pi}_{kl,h}\left[\mathbf{I}_h(\mathbf{v})\right]\,\mathrm{d}\gamma_{kl} \\
&= \int_{\gamma_{kl}} \boldsymbol{\mu}_{kl,h}\left(\left[\mathbf{I}_h(\mathbf{v})\right] - \left[\mathbf{I}_h(\mathbf{v})\right]\right)\,\mathrm{d}\gamma_{kl} = 0.
\end{aligned}
$$

We then have the following approximation result.

Proposition 5 (Approximation result)**.** *Under Assumptions 3 to 4 and if the mesh size is uniform between neighboring patches, any solution* $\mathbf{u}$ *of* (3) *which belongs to* $H^{r+1}(\Omega)^2$ *with* $1/2 < r \leq \min_{k,kl}(p_k, \eta(kl) + 1/2)$ *satisfies*

$$\inf_{\mathbf{v}_h \in \mathrm{Ker}(\mathbf{C}_h)} ||\mathbf{u} - \mathbf{v}_h||_V \leq C \sqrt{\sum_k h_k^{2r} ||\mathbf{u}||^2_{H^{r+1}(\Omega_k)^2}}. \qquad \square$$

Proof. By construction of $\mathbf{P}_h(\mathbf{u}) \in \mathrm{Ker}(\mathbf{C}_h)$, we have

$$\begin{aligned} \inf_{\mathbf{v}_h \in \mathrm{Ker}(\mathbf{C}_h)} ||\mathbf{u} - \mathbf{v}_h||_V &\leq ||\mathbf{u} - \mathbf{P}_h(\mathbf{u})||_V, \\ &\leq ||\mathbf{u} - \mathbf{I}_h(\mathbf{u})||_V + \sum_{k>l} ||\mathbf{E}_{kl,h} \circ \mathbf{\Pi}_{kl,h} \left[\mathbf{I}_h(\mathbf{u})\right]||_V. \end{aligned}$$

The last term in the above inequality is estimated as in [36, 40]. The result follows by sommation and by using Lemma 1 on $||\mathbf{u} - \mathbf{I}_h(\mathbf{u})||_V$. ■

5.3.4. Convergence result

We can now bound the error between the continuous and the discrete multipatch solution using the approach of [18, Theorem 6].

Theorem 6 (Convergence result)**.** *Under Assumptions 1 to 5 and if the mesh size is uniform between neighboring patches , the error between the solution* $\mathbf{u}$ *of* (3) *and the discrete solution* $\mathbf{u}_h \in \mathrm{Ker}(\mathbf{C}_h)$ *of* (8) *is bounded by*

$$||\mathbf{u} - \mathbf{u}_h||^2_V \leq C \sum_k h_k^{2r} ||\mathbf{u}||^2_{H^{r+1}(\Omega_k)^2},$$

with $||\mathbf{u}||^2_{H^{r+1}(\Omega_k)^2} = ||\mathbf{u}_p||^2_{H^{r+1}(\Omega_k)} + ||\theta||^2_{H^{r+1}(\Omega_k)}$. $\square$

Proof. The proof follows by a direct application of the Strang's second lemma. From the equivalence between the energy norm and the broken V norm, we have indeed

$$||\mathbf{u} - \mathbf{u}_h||_V \leq C_1 \left(\inf_{\mathbf{v}_h \in \mathrm{Ker}(\mathbf{C}_h)} ||\mathbf{u} - \mathbf{v}_h||_V + \sup_{\mathbf{w}_h \in \mathrm{Ker}(\mathbf{C}_h)} \frac{|a(\mathbf{u}, \mathbf{w}_h) - L(\mathbf{w}_h)|}{||\mathbf{w}_h||_V} \right),$$

and the result follows then from the consistency result in Proposition 4 and approximation result in Proposition 5. ■

5.4. Construction of the dual space

The simplest and natural choice is to use the same basis functions on each interface γ_{kl} for the primal (slave) and dual variables (p/p coupling). But due to cross points, the stability condition 3 is violated because of a local excess of dual variables at these points (see Figure 5). Moreover, the problem of cross points is particularly difficult in isogeometric analysis for geometrically non-conforming situations, since IGA is not interpolating at internal points, and therefore the displacement value at cross points may not be uniquely defined.

Two solutions can be proposed to overcome this difficulty [26]. The first one is to coarsen the mesh of the dual space next to the cross points. The alternative, valid for slave conforming situations, is to locally reduce the order of approximation of the dual finite elements which are adjacent to the cross points as done in [18] for 3D problems. This local dimension reduction results in a modified B-spline basis $\tilde{N}_i^p$ given by [18]

$$\tilde{N}_i^p(\xi) = \begin{cases} N_i^p(\xi) + \alpha_i N_1^p(\xi), & \forall i \in \{2, \dots, p+1\}, \\ N_i^p(\xi), & \forall i \in \{p+2, \dots, n-p-1\}, \\ N_i^p(\xi) + \beta_i N_n^p(\xi), & \forall i \in \{n-p, \dots, n-1\}, \end{cases}$$

where the coefficients α_i and β_i are constructed in order to achieve an approximation of order $p-1$ and partition of unity next to the cross points. For quasi-uniform meshes (Assumption 2), these coefficients are bounded and one can prove that the inf-sup Assumption 3 and the approximation condition 4 hold in this case [18].

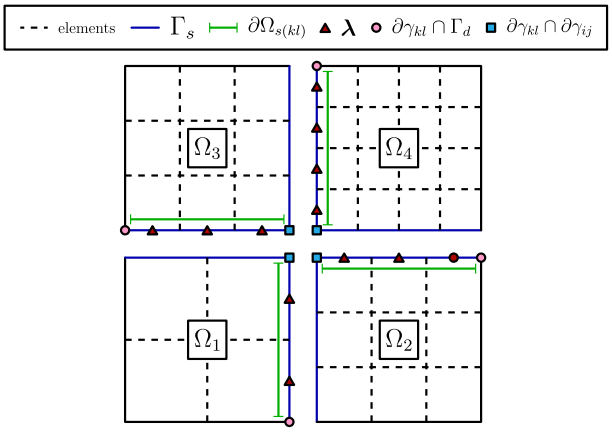

Figure 5: Quadratic dual space for the clamped four patches problem. The dual nodes are built on the slave sides (Ω_1 for γ_{21}, Ω_2 for γ_{42}, Ω_3 for γ_{31} and Ω_4 for γ_{43}). Before correction, there are four dual nodes at center.

The identification of the elements adjacent to cross points and the construction of the coefficients α and β can nevertheless be cumbersome in practice as illustrated in Section 7.6 on a typical example. Therefore, we will also propose herein a simpler variant well adapted to the complex geometries encountered in industry, where we simply suppress all dual degrees of freedom which are located at corners of the slave domain (Figure 6)

$$M_{kl}^{\text{ind}} = \{\mathbf{w} \in \text{Tr}_{kl} V_{s(kl),h}, \mathbf{w}_A = \mathbf{0}, \text{ at all corners } A \in \Omega_{s(kl)}\}. \tag{9}$$

For the slave conforming situation where we have $M_{kl,h}^{\text{ind}} = W_{kl,h}$, this choice trivially satisfies the inf-sup Assumption 3 at the cost of a loss of optimality in the approximation of the Lagrange multipliers, as indicated below.

Proposition 7. *For slave conforming partitions, the simple choice $M_{kl,h}^{\text{ind}} = W_{kl,h}$ satisfies*

$$\inf_{\boldsymbol{\mu}_{kl} \in M_{kl}^{\text{ind}}} \sup_{\mathbf{w}_k \in W_{kl,h}} \frac{\displaystyle\int_{\gamma_{kl}} \mathbf{w}_k \boldsymbol{\mu}_{kl} \, \mathrm{d}\gamma_{kl}}{||\mathbf{w}_k||_{L^2(\gamma_{kl})^2} ||\boldsymbol{\mu}_{kl}||_{L^2(\gamma_{kl})^2}} = 1, \tag{10}$$

$$\inf_{\boldsymbol{\mu}_{kl} \in M_{kl,h}^{\text{ind}}} ||\boldsymbol{\lambda} - \boldsymbol{\mu}_{kl}||_{L^2(\gamma_{kl})^2} \leq C h_k ||\boldsymbol{\lambda}||_{H^1(\gamma_{kl})^2} + C h_k^{1/2} ||\boldsymbol{\lambda}||_{H^1(\gamma_{kl})^2}. \qquad \square$$

Proof. By construction, we have $W_{kl,h} \equiv M_{kl,h}^{\text{ind}}$. Hence, taking $\text{Tr}_{kl} \mathbf{w}_k = \boldsymbol{\mu}_{kl}$, we get (10) with $C_2 = 1$. For the second line, without loss of generality, we take $\gamma_{kl} = (0, 1)$ and introduce

$$\boldsymbol{\mu}_{kl} = r_h(\boldsymbol{\lambda}) - \lambda(0) N_1^p - \lambda(1) N_n^p$$

where $r_h(\boldsymbol{\lambda})$ denotes the interpolation operator from $H^1(0,1)^2$ into $M_{(0,1),h}^{\text{ind}} = \text{span}_{i \in [\![1,n]\!]} \left\{ N_i^p \right\}$. From the triangular inequality, we have

$$||\boldsymbol{\lambda} - \boldsymbol{\mu}_{kl}||_{L^2(0,1)^2} \leq ||\boldsymbol{\lambda} - r_h(\boldsymbol{\lambda})||_{L^2(0,1)^2} + |\lambda(0)| \cdot ||N_1^p||_{L^2(0,h)^2} + |\lambda(1)| \cdot ||N_n^p||_{L^2(1-h,1)^2}.$$

For one dimensional domain, we have classically

$$\begin{aligned}
&||\boldsymbol{\lambda} - r_h(\boldsymbol{\lambda})||_{L^2(0,1)^2} \leq C h ||\nabla \boldsymbol{\lambda}||_{L^2(0,1)^2}, \\
&\max_{x \in [0,1]} |\boldsymbol{\lambda}(x)| \leq C ||\boldsymbol{\lambda}||_{H^1(0,1)^2}, \\
&||N_i^p||_{L^2((i-1)h,ih)}^2 = h ||\widehat{N}_i^p||_{L^2(0,1)}^2,
\end{aligned}$$

which yields the desired result. ■

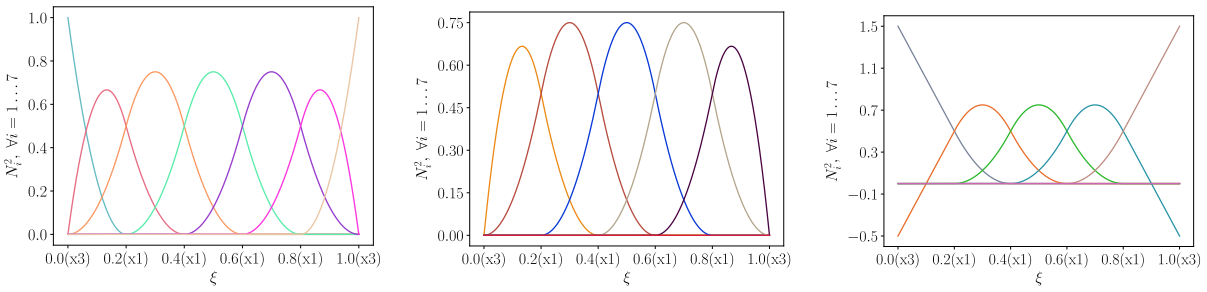

Figure 6: Comparison of basis for the dual space. Left: original. Center: simplified $M^{\text{ind}} = \text{span}_{i\in[\![2,n-1]\!]}\left\{N_i^p(\xi)\right\}$. Right: optimal $M^{\text{opt}} = \text{span}_{i\in[\![2,n-1]\!]}\left\{\tilde{N}_i^p(\xi)\right\}$. Quadratic elements $p = 2$ with seven basis functions $n = 7$. One can observe that for the simplified choice, the multipliers are zero at cross points, which simplifies the inf-sup verification, but leads to a degradation of accuracy for the interface multipliers. The degradation will be attenuated for the augmented lagrangian choice.

6. Reduced integration and stability

6.1. Normals reconstruction

The displacements in (1) are represented using an exact normal $\mathbf{n}$ given by

$$\mathbf{n}(\xi,\eta) = \frac{\mathbf{x}_{,\xi}\times\mathbf{x}_{,\eta}}{||\mathbf{x}_{,\xi}\times\mathbf{x}_{,\eta}||_2},$$

with $\mathbf{x}_{,\xi}$ and $\mathbf{x}_{,\eta}$ the local covariant vectors. The derivatives $\boldsymbol{\nabla}_{\boldsymbol{\xi}}\mathbf{n} = \begin{bmatrix}\mathbf{n}_{,\xi} & \mathbf{n}_{,\eta} & \mathbf{0}\end{bmatrix}$ will then involve involve the second order derivatives of the geometry, that is second order derivatives of NURBS $R_A(\xi,\eta)$ which can be incompatible with the use of a reduced quadrature rule. This is why we propose to use in (1) an interpolation based construction, namely

$$\mathbf{n}(\xi,\eta) \approx \mathbf{n}^h(\xi,\eta) = \sum_{A=1}^{n\cdot m} R_A(\xi,\eta)\mathbf{n}_A, \tag{11}$$

using normals $\mathbf{n}_A$ constructed at given collocation points. An inherent difficulty from IGA is that control points are not necessary interpolant, and thus may not be on the shell surface. Consequently, we have to carefully define the collocation points in this construction. As detailed in [19], an orthogonal projection of control points on mid-surface or defining equally spaced normals in the parameter space respectively present a high computational cost and a lack of precision. Based on the analysis performed in [19, Section 3.4] our choice herein uses the relation (11) defining the control normals $\mathbf{n}_A$ at Greville abscissae [41]

$$\bar{\xi}_k = \frac{1}{p}\sum_{i=1}^{p}\xi_{k+i},\ \forall k \in [\![1,n]\!].$$

These abscissae will correspond to the maxima of the basis functions as shown in Figure 7. With this construction, the normals in (11) are constructed by

$$\mathbf{n}^h(\boldsymbol{\xi}) = \sum_{A=1}^{n\cdot m} R_A(\boldsymbol{\xi})\frac{\mathbf{x}_{,\xi}(\bar{\boldsymbol{\xi}}_A)\times\mathbf{x}_{,\eta}(\bar{\boldsymbol{\xi}}_A)}{||\mathbf{x}_{,\xi}(\bar{\boldsymbol{\xi}}_A)\times\mathbf{x}_{,\eta}(\bar{\boldsymbol{\xi}}_A)||_2} = \sum_{A=1}^{n\cdot m} R_A(\boldsymbol{\xi})\mathbf{n}(\bar{\boldsymbol{\xi}}_A) = \sum_{A=1}^{n\cdot m} R_A(\boldsymbol{\xi})\mathbf{n}_A. \tag{12}$$

With this last relation, the derivatives $\boldsymbol{\nabla}_{\boldsymbol{\xi}}\mathbf{n}^h = \begin{bmatrix}\mathbf{n}^h_{,\xi} & \mathbf{n}^h_{,\eta} & \mathbf{0}\end{bmatrix}$ only require the first derivatives of $R_A(\xi,\eta)$, which means a lower computational cost and a compatibility with a reduced integration [19].

6.2. Reduced integration

An advantage of IGA is that the exact representation of a smooth geometry gives us the possibility to define an accurate normal all over the shell (excluding points where the continuity is reduced). But it is also now well-known

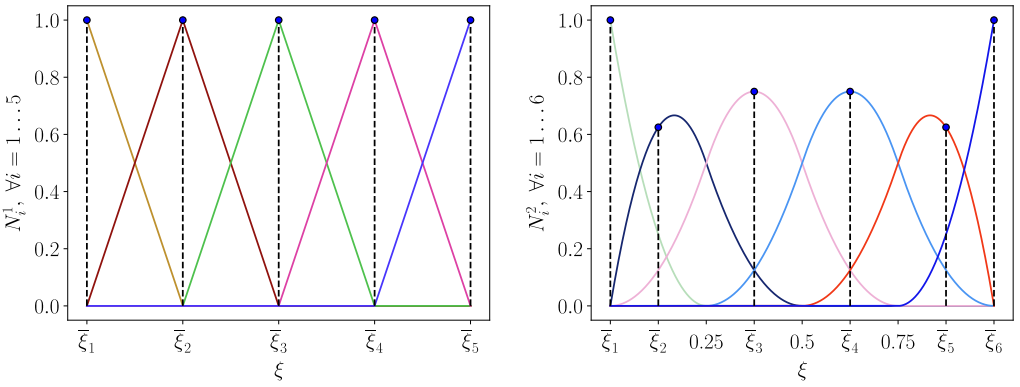

Figure 7: Greville abscissae denoted by bullet points. Left: linear functions. Right: quadratic functions.

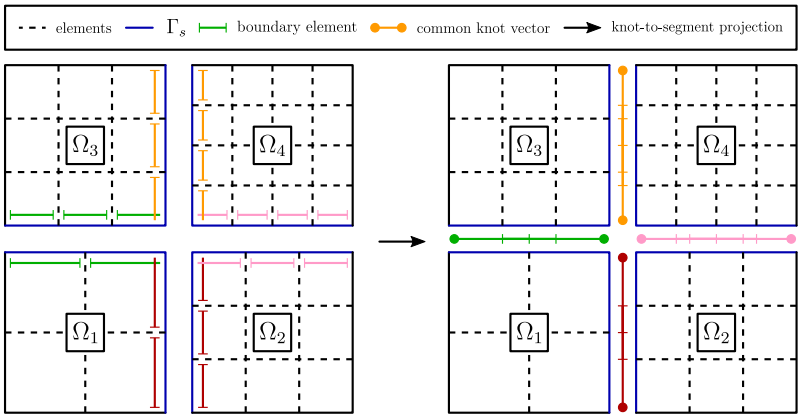

Figure 8: Creation of common knots vectors for each interface. After knot-to-segment projection, we get a subdivided parent grid built on this extended set of common knot vectors, with four elements for γ_{21} and γ_{31} and six elements for γ_{42} and γ_{43} .

that thick shell elements are suffering from numerical locking and some examples are given in [42, 43] for low order Lagrange polynomials. This membrane and shear locking are due to a conflict of order between the different terms composing the strain energy and despite of the high regularity allowed by NURBS functions, IGA is also suffering from locking [44]. An elevation of order (p-refinement) can reduce this locking at the cost of an higher computational time [45]. Here we overcome this difficulty by extending the reduced quadrature rule, given in [19], to multipatch geometries. This rule lowers the number of integration points by one in each direction in corners elements and by $r_k + 1$ in inner elements by taking advantage of the higher r_k regularity between elements brought by IGA. Then, using exact normals is incompatible with the proposed reduced integration because as seen earlier introducing exact normals require to calculate first and second derivatives of the position vector. Therefore, we will use the reconstructed normals introduced in (11). Last, we will use a similar reduced integration for the interface coupling terms. The integration of the coupling terms is to be performed on a common parent space. In order to do that, we perform a symmetric knot-to-segment (KTS) projection for all knots vectors on both sides of the interfaces γ_{kl} building a subdivision of the parent space. An example of KTS projections, represented in the physical space, is given on Figure 8 for a plate made of four patches.

The mortar integrals and penalty terms can then be evaluated on each element joining two successive knots of the common parent space, i.e., on four elements for $\tilde{\gamma}_{21}$ and $\tilde{\gamma}_{31}$ and six elements for $\tilde{\gamma}_{42}$ and $\tilde{\gamma}_{43}$. Noting by p_k and p_l the order of the basis functions for the patches Ω_k and Ω_l, a complete quadrature rule for each element of $\tilde{\gamma}_{kl}$ would require $n_{\text{GPC}} = \text{E}_{\text{sup}}\left[\frac{(p_k+p_l)+1}{2}\right]$ integration points. To reduce the computational cost, we will proceed as for the patch

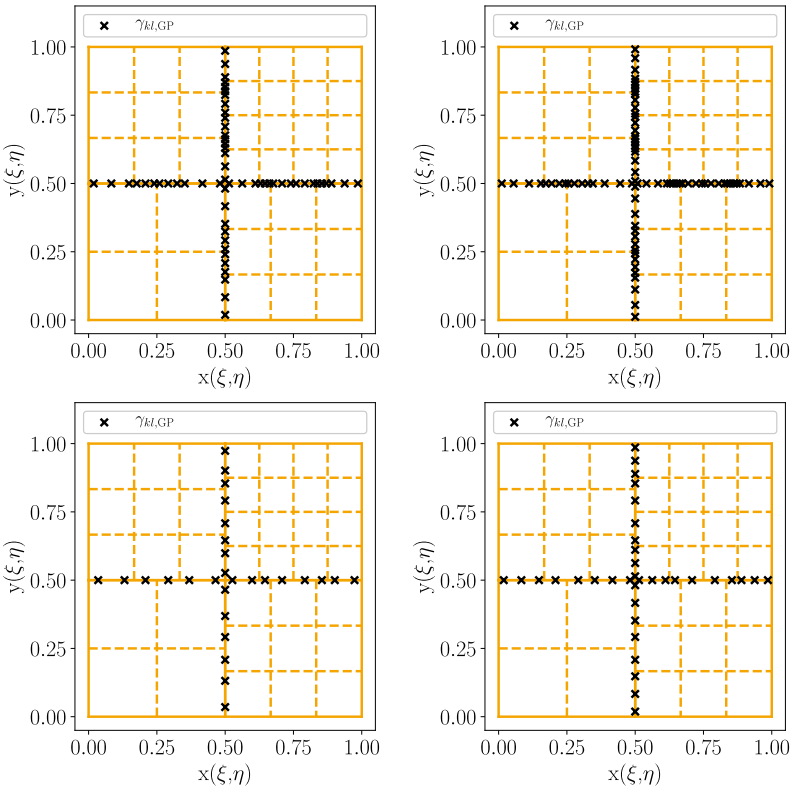

Figure 9: Quadrature rules for four interfaces using the common knots of Figure 8. Left: quadratic functions. Right: cubic functions. Top: complete integration. Bottom: reduced integration.The reduced integration is used both for the dual and for the penalty terms.

integration, by taking $n_{\text{GPC}} - 1$ points at each end of the common knots vector and one point otherwise (Figure 9).

6.3. Numerical evaluation of the stability

In order to validate numerically the relevance of the above discretization choices, we begin by looking at the stability of our discrete problem (8). In a matrix form, this problem writes [39]

$$\begin{bmatrix} \mathbf{K}_{\text{struc}} & \mathbf{C}^{\lambda} \\ (\mathbf{C}^{\lambda})^T & \mathbf{0} \end{bmatrix} \begin{bmatrix} \mathbf{u} \\ \lambda \end{bmatrix} = \begin{bmatrix} \mathbf{F} \\ \mathbf{0} \end{bmatrix}.$$

Let $\mathbf{Q}$ be the matrix associated to the interface L^2 scalar product

$$\lambda^T \mathbf{Q} \boldsymbol{\mu} = \int_{\Gamma_s} \lambda^h \boldsymbol{\mu}^h \, \mathrm{d}\Gamma_s, \ \forall (\lambda^h, \boldsymbol{\mu}^h) \in \boldsymbol{M}_h,$$

and introduce the product norm

$$\mathbf{N} = \mathbf{K}_{\text{struc}} \bigoplus \mathbf{Q} = \begin{bmatrix} \mathbf{K}_{\text{struc}} & \mathbf{0} \\ \mathbf{0} & \mathbf{Q} \end{bmatrix}.$$

Following [39], the numerical stability of (8) is characterized by the lowest norm negative eigenvalue σ_{min} of the discrete problem

$$\mathbf{KU} = \sigma \mathbf{NU}.$$

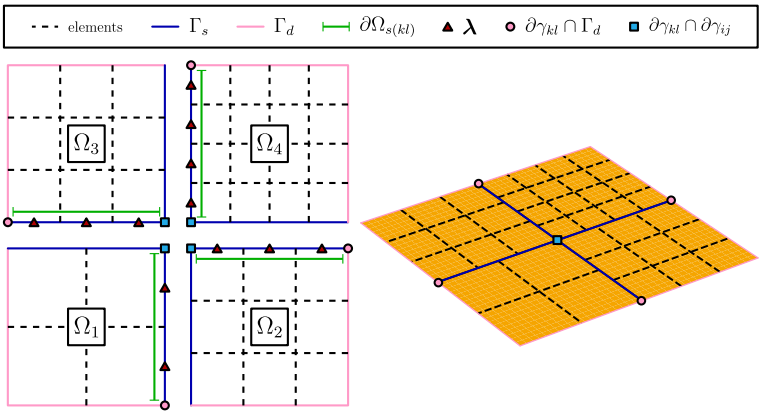

Figure 10: Clamped shell model problem used for numerical stability analysis. The four patches are geometrically compatible, but their discretisation are not.

In more details, after elimination of λ from this eigenvalue problem, one can check that $|\sigma^2_{min} - \sigma_{min}|$ is equal to the lowest positive eigenvalue s_{min} of the reduced eigenproblem [39, Theorem 4]

$$\mathbf{C}^{\lambda}\mathbf{Q}^{-1}(\mathbf{C}^{\lambda})^T\mathbf{u} = s\mathbf{K}_{\text{struc}}\mathbf{u},$$

which also writes after division by $\alpha(h)$

$$\mathbf{C}^{\lambda}\mathbf{Q}_h^{-1}(\mathbf{C}^{\lambda})^T\mathbf{u} = \frac{s}{\alpha(h)}\mathbf{K}_{\text{struc}}\mathbf{u}, \tag{13}$$

where we have introduced the matrix $\mathbf{Q}_h = \alpha_h\mathbf{Q}$ of the $\alpha(h)$ weighted L^2 product. In particular the choice of $\alpha(h) = h$ leads to the discrete norm $||\cdot||_{-1/2,h}$ introduced by [36] in their analysis of the mortar elements. From [39, Theorem 2], we then obtain the global inf-sup estimate

$$\inf_{\boldsymbol{\mu}\in M_h}\sup_{\mathbf{v}\in V_h}\frac{\mathbf{v}^T\mathbf{C}^{\lambda}\boldsymbol{\mu}}{||\mathbf{v}||_{\text{struc}}||\boldsymbol{\mu}||_h} = \sqrt{\frac{s_{min}}{\alpha(h)}} = \sqrt{\frac{|\sigma^2_{min} - \sigma_{min}|}{\alpha(h)}}, \tag{14}$$

after endowing V_h and M_h with the structural energy norm $||\cdot||_{\text{struc}}$ and $\alpha(h)$ weighted L^2 norm $||\cdot||_h$ respectively.

We check this stability of a four patches clamped shell model problem (Figure 10). Four values of the thickness t are considered $t \in \left\{10^{-4}, 10^{-3}, 10^{-2}, 10^{-1}\right\}$ (m). The global inf-sup estimate using the discrete norm $||\cdot||_{-1/2,h}$ is evaluated according to its h-dependency (Figure 11) and p-dependency (Figure 12).

We remark that when the shear contribution is taken into account (which correspond to the two plots on the top for the h-dependency and p-dependency cases), there is a clear sensitivity to the thickness at order $\mathcal{O}(t^2)$. This sensitivity is due to the underlying treatment of the shear coefficients in a thick shell model which introduces very large shear stiffness in the structural stiffness $\mathbf{K}_{\text{struc}}$, hence modifying the right hand side of the eigenvalue problem (13). If we now approach the space corresponding to the zero shear energy (i.e. multiplying by t^2 the shear contribution), we are able to suppress these shear spurious modes and we obtain a global inf-sup estimate totally independent of the thickness t, also observing the overall stability of our discretisation strategy with inf-sup values bounded away from zero and quasi independent of the discretisation parameters.

7. Numerical results

We herein propose to validate both the multipatch formulations and the quadrature rules on academic and industrial examples. The numerical implementation was performed in Python with a LLVM-based just-in-time compiler Numba [46]. Matrix are stored in a sparse CSR format thanks to the SciPy package [47]. This choice allows us to use efficient

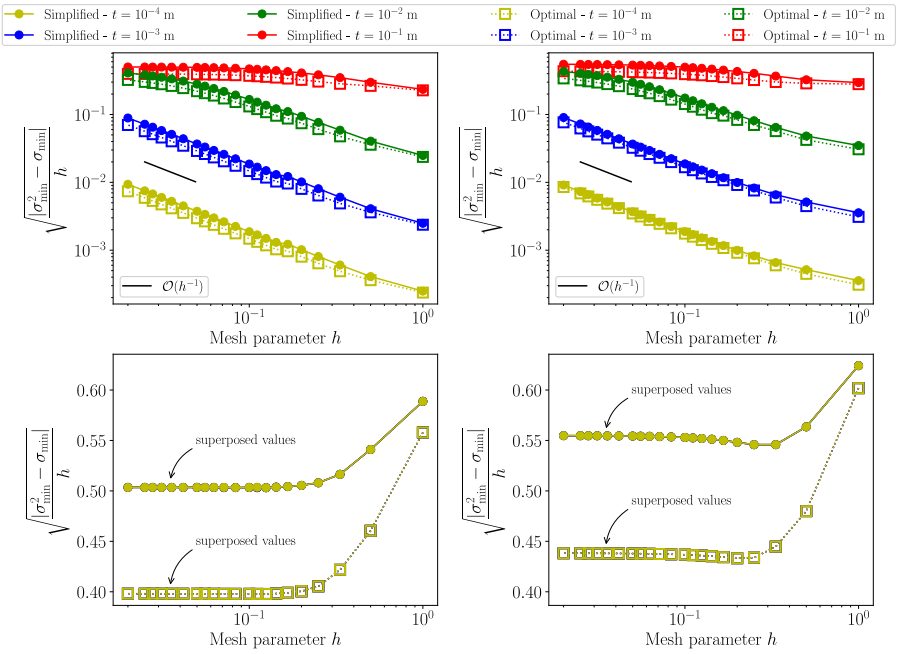

Figure 11: Evolution of the global stability constant as function of the thickness and the mesh size with an approximation order $p = 2$. Four values of the thickness t are considered $t \in \{10^{-4}, 10^{-3}, 10^{-2}, 10^{-1}\}$ (m). Left: complete integration. Right: reduced integration. Top: shear contribution is taken into account. Bottom: the shear contribution is corrected by multipliying the shear terms by t^2.

linear solvers such as Pardiso [48] for the structural analysis or Lanczos, included in the ARPACK package [49], for the eigenvalue analysis. We use the following notation to describe the considered element and quadrature rule

$$\text{RM } \underline{(1)}\ \underline{(2)}\ \text{C } \underline{(3)}\ \underline{(4)} \begin{cases} (1) : \text{P or S for plate or shell element,} \\ (2) : \text{order of the basis functions,} \\ (3) : \text{regularity of the basis functions,} \\ (4) : \ \ldots \text{ or R for complete or reduced integration.} \end{cases}$$

As an example, the element RMP3C1 corresponds to a Reissner-Mindlin plate with cubic shape functions and C^1 inter-element continuity associated to a complete quadrature rule. Moreover, a plate element will have five DOF that is three displacements and two rotations, and a shell element will have six DOF including three rotations.

7.1. Simply supported plate

7.1.1. Validation

The first study concerns a plate of edge length L and width l which is simply supported on its external borders Γ_d and submitted to a concentrated load F at its center, see Figure 13. The structure is built with four patches having a cross point at the center due to the intersection of the four interfaces. We use a first order approximation of the problem by separating the strain in membrane, bending and transverse shear parts as follows

$$\mathbf{e}_m = \begin{bmatrix} u_{,x} \\ v_{,y} \\ 0 \\ u_{,y} + v_{,x} \\ 0 \\ 0 \end{bmatrix}, \quad \boldsymbol{\chi}_b = \begin{bmatrix} z\theta_{y,x} \\ -z\theta_{x,y} \\ 0 \\ z(\theta_{y,y} - \theta_{x,x}) \\ 0 \\ 0 \end{bmatrix}, \quad \boldsymbol{\gamma}_s = \begin{bmatrix} 0 \\ 0 \\ 0 \\ 0 \\ w_{,y} - \theta_x \\ w_{,x} + \theta_y \end{bmatrix},$$

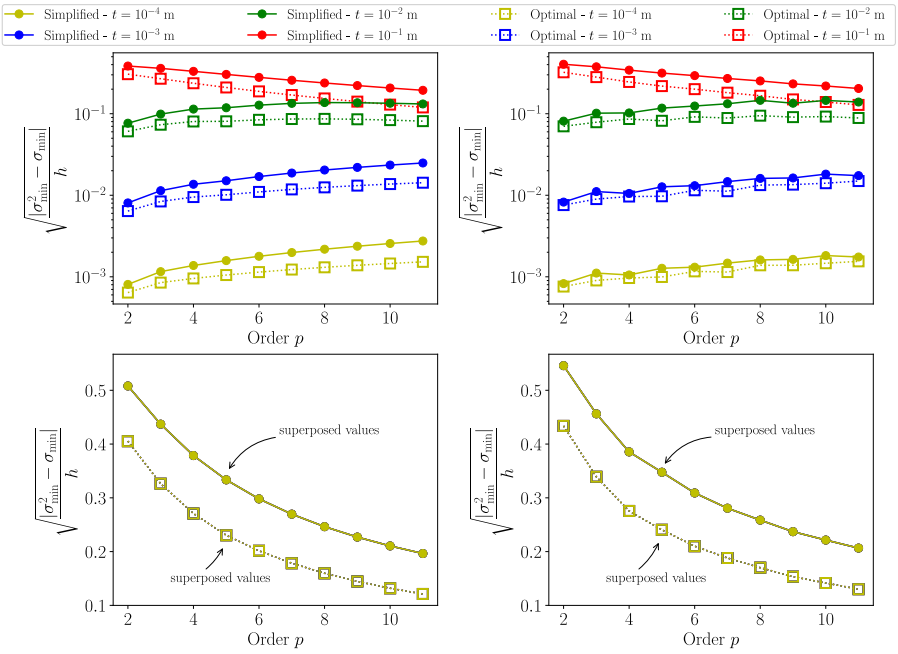

Figure 12: Evolution of the global stability constant as function of the thickness and the approximation order with a mesh size $h = 0.25$. Four values of the thickness t are considered $t \in \{10^{-4}, 10^{-3}, 10^{-2}, 10^{-1}\}$ (m). Left: complete integration. Right: reduced integration. Top: shear contribution is taken into account. Bottom: shear contribution is neglected by multipliying the shear part by t^2.

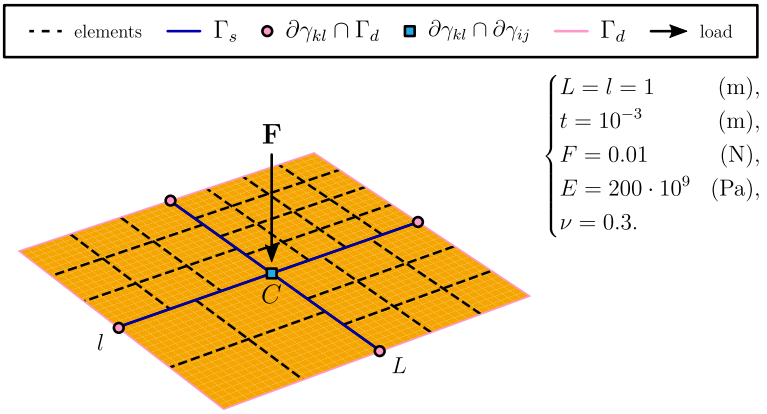

Figure 13: Geometry description and physical properties for a simply supported plate. Four geometrically conforming patches with incompatible discretisation ranging from four to sixteen elements are used.

by neglecting the membrane part and only considering the out-of-plane displacement w and the two rotations θ_x and θ_y. Consequently, we have a pure bending problem which can only be affected by transverse shear locking. The analytical solution for an equivalent Kirchhoff-Love problem was obtained introducing decomposition solution series in [50, 51]. The maximum displacement at the center of the plate is thus

$$w_C = w\left(\frac{L}{2}, \frac{l}{2}\right) = \frac{48F(1-\nu^2)}{\pi^4 E t^3 L l} \sum_{m=0}^{\infty} \sum_{n=0}^{\infty} \frac{1}{\left(\left(\frac{2m+1}{L}\right)^2 + \left(\frac{2n+1}{l}\right)^2\right)^2}.$$

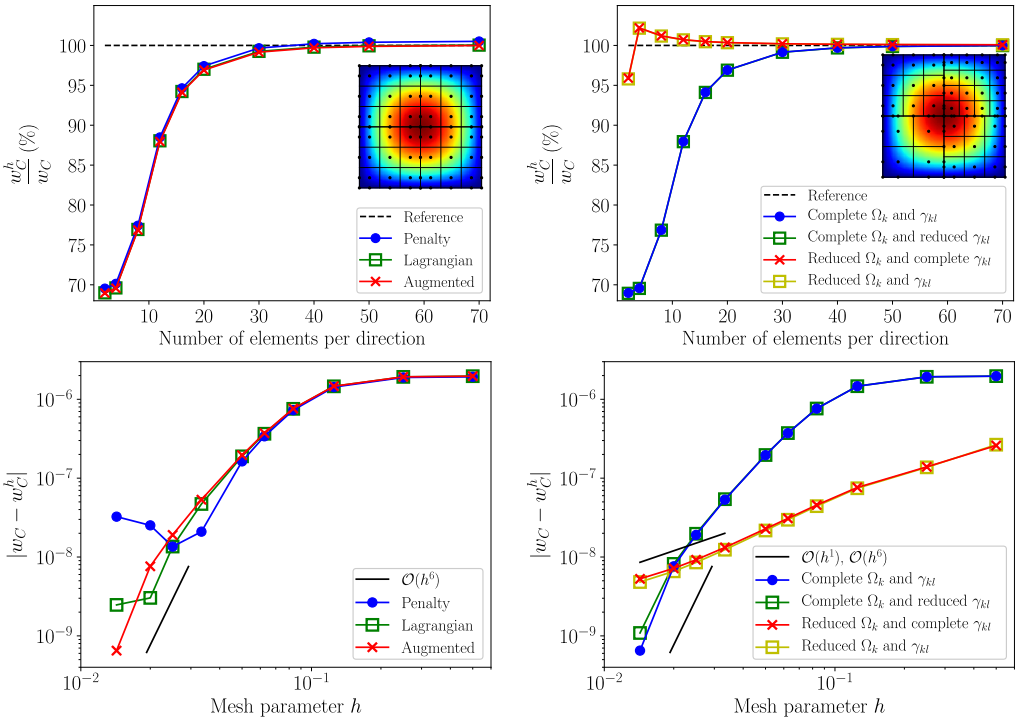

Figure 14: Displacement for the simply supported plate with quadratic NURBS. Left: multipatch methods and complete integration. Right: quadrature rules and augmented method. Top: ratio w_C^h/w_C. Bottom: error $|w_C - w_C^h|$. It can be highlighted from the two right figures, using the augmented approach, that no difference is observed between a complete and reduced quadrature rule on the interfaces kl, only the computational cost is affected. However, choosing the reduced integration in each patch k leads to a significantly reduced transverse shear locking.

The first results, using quadratic NURBS and the simplified mortar approach, are shown on Figure 14. The ratio w_C^h/w_C, between the discrete solution and the analytical one, is plotted according to the number of elements per direction for different multipatch formulations and quadrature rules. The discrete solution w_C^h is obtained by taking the mean value of the four control points located at the center C. The error $|w_C - w_C^h|$ is shown, depending on the mesh parameter h, again for different multipatch methods and integrations. For the primal and augmented methods, the penalty factor is set to $\alpha_{kl} = 10^3 \cdot E$. An example of out-of-plane displacement can be visualized for conforming meshes (top-left) or non-conforming meshes (top-right). We can see from the left figures that the three multipatch methods, with a complete integration, are showing similar results except for the penalty formulation. This last point was expected because this method is variationally inconsistent on α_{kl}. In fact, fixing the penalty factor to a constant value does not provide an exact enforcement of the continuity constraint. The augmented lagrangian method using the simplified mortar space is the most efficient.

It can be highlighted from the two right figures, using the augmented approach, that no difference is observed between a complete and reduced quadrature rule on the interfaces γ_{kl}, only the computational cost is affected. However, choosing the reduced integration in each patch Ω_k leads to a significantly reduced transverse shear locking.

7.1.2. Simplified and optimal approaches

We now want to compare the simplified mortar space to the optimal one proposed in [18]. The solutions for a dual and augmented approaches are given on Figure 15 for a complete and reduced integration with shape functions of order $p = 2$ to $p = 4$. We recall that for the simplified approach the dual space is not of optimal order with an additional term in $\sqrt{h}$ appearing in the convergence estimate . This is a consequence for the non respect of the partition of unity on the elements that support the interpolant shape functions at singular points. Consequently, we can see differences between the simplified and optimal approaches when using the dual formulation. However, this difference gets very

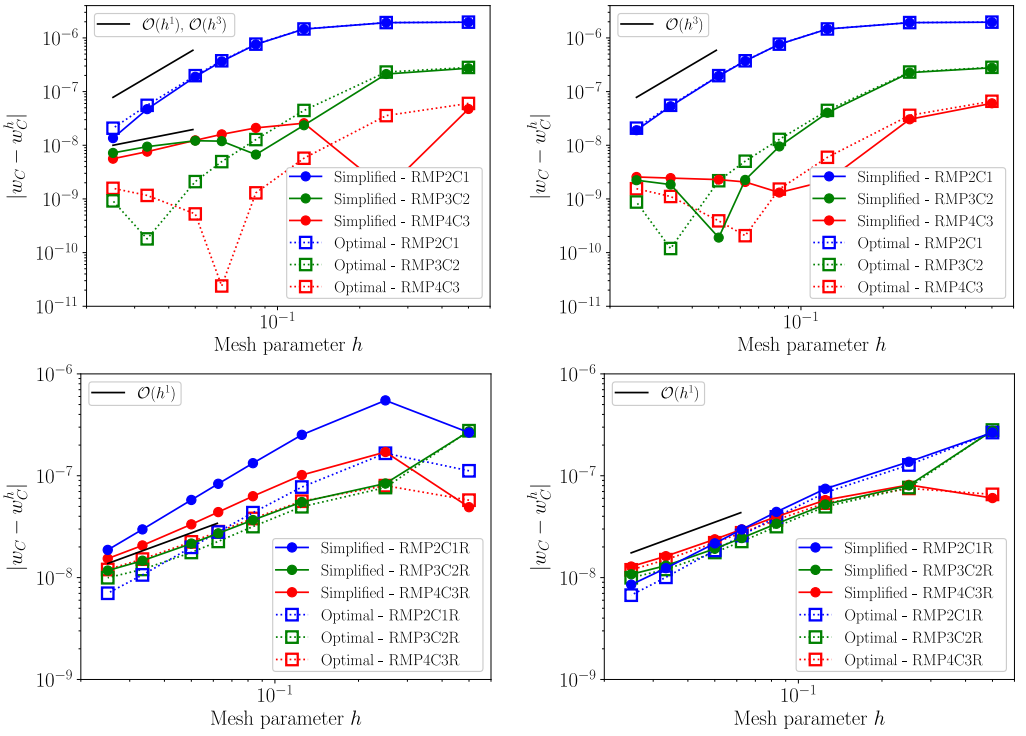

Figure 15: Simplified and optimal mortar methods for the simply supported plate. Left: dual approach. Right: augmented approach. Top: complete integration. Bottom: reduced integration.

small when using the augmented formulation. Adding a regularization primal term allows us to enforce locally, near each singular point, the continuity constraint.

7.1.3. Influence of the penalty factor

Above, the penalty factor was set to $\alpha_{kl} = 10^3 \cdot E$ for the primal and augmented methods. This factor may look large, particularly for the augmented approach, and so a further study is necessary. As we are comparing the values of w_C^h at the center of the plate (cross point), a strong coupling condition at this location is required. Consequently, the influence of the penalty factor will not be negligible for the simplified approach. The error $|w_C - w_C^h|$ is shown on Figure 16 for the two quadrature rules and three different mesh parameters h with a penalty factor $\alpha_{kl} \in \left[10^{-6} \cdot E, 10^6 \cdot E\right]$. As expected, the influence of the penalty factor is noticeable for the simplified approach whereas it is negligible for the optimal one. Concerning the complete quadrature rule (domains and interfaces), the shear locking is particularly visible for the finer meshes and the error can increase for the largest penalty factors. In this case, the simplified dual approach artificially produces a misleading low error. It is no longer true for the reduced integration (applied for each patch and interface) which can alleviate this locking phenomenon. The augmented lagrangian method with the simplified mortar space exhibits the same accuracy as the dual/augmented optimal methods for a penalty factor $\alpha_{kl} \geq 10 \cdot E/h$. This value was used for the other studies of the plate.

7.1.4. Thickness dependency

The reduced quadrature rule, applied here in each domain and for each interface, should lead to a solution independent of the thickness t, if we have no shear locking. As the analytical solution is only valid for Kirchhoff-Love elements, we make the slenderness ratio L/t vary in our tests from a moderate thin plate $L/t = 10^3$ to a very thin plate $L/h = 10^5$. A thickness dependant load $F = 10^7 \cdot t^3$ is applied in order to keep a constant transverse displacement w_C. Considering the two quadrature rules and the three multipatch methods (including the simplified and optimal variants) with a penalty factor $\alpha_{kl} \approx 30 \cdot E/h$, the error $|w_C - w_C^h|$ is plotted on Figure 17. As stated in [19] for monopatch structures, the complete integration leads to an artificial solution dependency on t and and obviously it is still the case

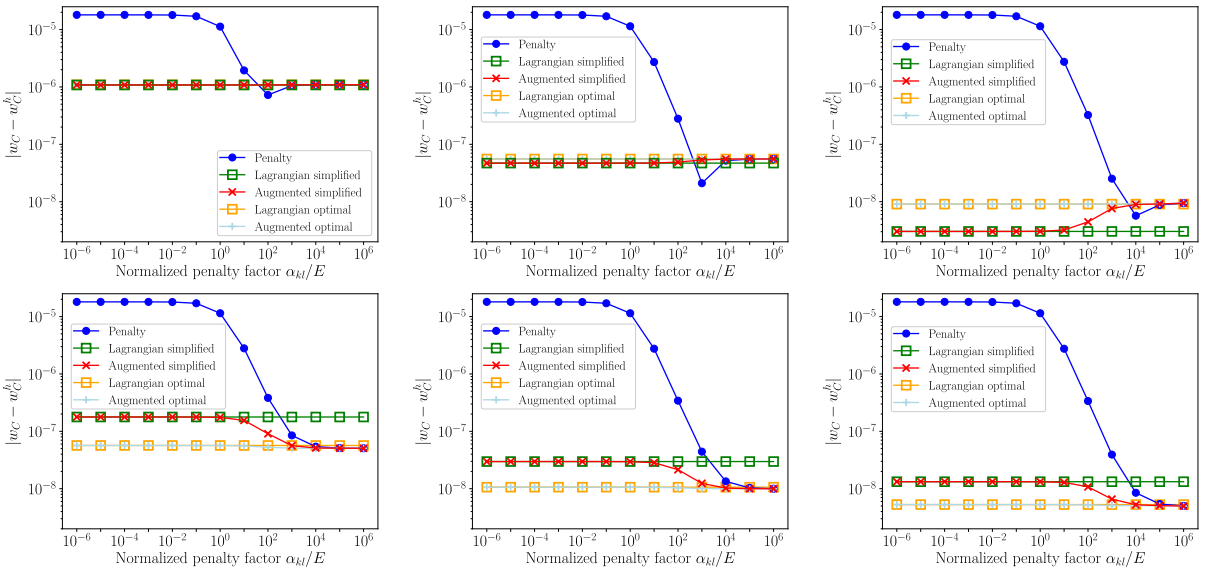

Figure 16: Influence of the penalty factor for the simply supported plate with quadratic NURBS. From left to right: $h = 1/10$, $h = 1/30$ and $h = 1/50$. Top: complete integration. Bottom: reduced integration. The simplified construction of the mortar space leads to an accurate solution as soon as the penalty term goes above a certain moderate threshold. Observe also the presence of locking when using complete integration.

for multipatch geometries. The reduced quadrature rule avoids shear locking up to all practical purposes. A very slight locking may nevertheless subsist since, for some boundary conditions and in particular the simply supported one, fewer Gauss points could be used [19].

7.1.5. Natural frequency analysis

In order to validate the reduced quadrature rule detailed in [19] and implemented here for multipatch structures, we perform a modal analysis. This will further validate the multipatch methods and will also confirm that no spurious zero energy modes are generated. For this purpose, we are now considering the generalized eigenvalue problem

$$\begin{aligned} \rho\,\omega^2\mathbf{u} + \mathbf{div}(\boldsymbol{\sigma}) &= \mathbf{0} \quad \text{in } V, \\ \mathbf{u} &= \mathbf{0} \quad \text{on } \Gamma_d, \end{aligned}$$

where ρ stands for the density and ω is the natural frequency. We assume linear isotropic elasticity in plane stress. In addition to the previous physical properties reported on Figure 13, the density is set to $\rho = 7500\,\mathrm{kg.m^{-3}}$. After spatial discretization we have to solve

$$\mathbf{KU} = (\omega^h)^2\mathbf{MU}, \tag{15}$$

where $\mathbf{K}$ is the global stiffness matrix and $\mathbf{M}$ the global mass matrix

$$\mathbf{M} = \begin{bmatrix} \mathbf{M}_1 & \mathbf{0} & \mathbf{0} \\ \mathbf{0} & \ddots & \mathbf{0} \\ \mathbf{0} & \mathbf{0} & \mathbf{M}_K \end{bmatrix}.$$

It has been shown in [19] that, with the considered reduced integration, no zero energy modes were obtained if a sufficient number of Gauss points was considered at each extremity of the patch, i.e., at locations where there is an accumulation of basis functions. This should remain valid for multipatch geometries.

The geometry under study is the same as for the structural analysis but the plate is now clamped on its external boundaries. The first eigenvalue ω_1^h is compared on Figure 18 to the analytical one ω_1, taken from [52], for different multipatch methods and quadrature rules all used with the simplified construction of the dual space. We are using

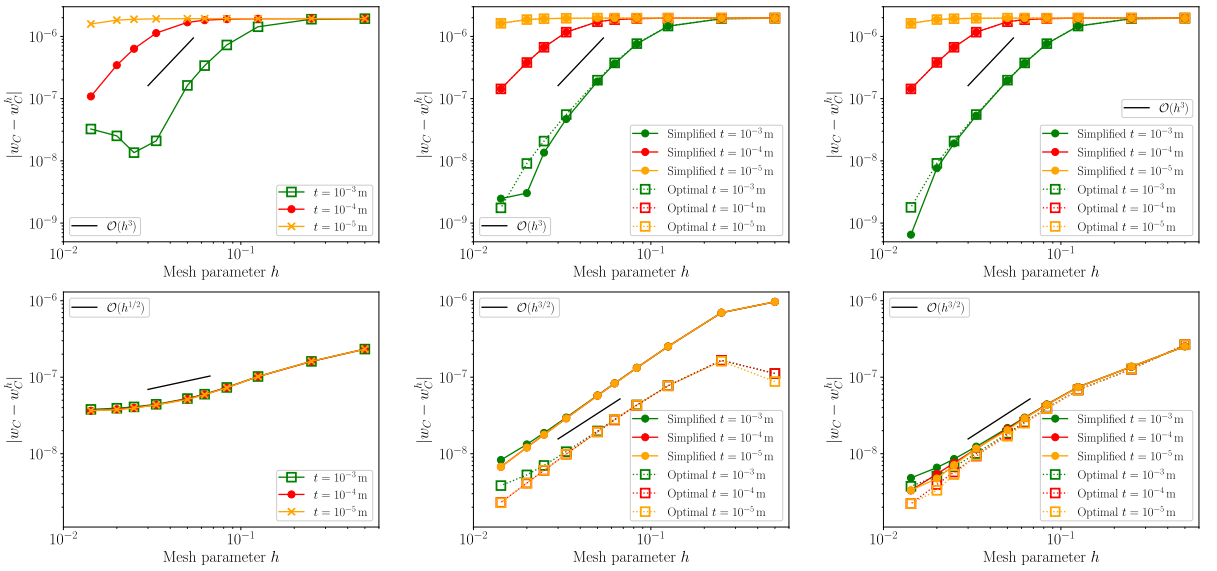

Figure 17: Influence of the thickness for the simply supported plate with quadratic NURBS. From left to right: primal, dual and augmented multipatch methods. Top: complete integration. Bottom: reduced integration. A clear thickness dependent shear locking is observed as in [19] when using full integration inside the patches.

quadratic NURBS on the left and cubic functions on the right. A numerical reference, taken from Abaqus Finite Element software is also considered for comparison.

An example of solution can be visualised for conforming meshes (top-left) or non-conforming meshes (top-right). As for the structural analysis, the penalty method is less accurate than the dual or augmented method which both lead to the same results. The reduced integration can significantly reduce the locking for quadratic functions but is not necessary for cubic functions for which numerical locking is obviously less significant. We can add that, as previously mentioned, no hourglass modes are observed.

7.2. Pinched hemisphere

We are now considering a thick shell structure whose solution is sensitive to the construction strategy used for the surface normal. We use here the collocated normals introduced in (12). It has a good compromise between accuracy and computational cost and, moreover, it is compatible with our reduced integration rule. The geometry was taken from the well-known shell obstacle course which aims at validating shell element, see [53, 54]. It is an hemisphere of radius R with a 18° hole as shown on Figure 19.

The multipatch structure has four patches without singular points and is subjected to equal and opposite concentrated forces $\mathbf{F}$ applied at the four cardinal points of its equator. The rigid body motions are eliminated fixing two points of the upper edge and, apart from these points, the two ends are free. This test is characterized by inextensible bending modes and will guarantee that the element is not suffering from membrane or shear locking. We note u_A^h the horizontal displacement obtained at point A which will be compared to the analytical solution $u_A = 9.3 \cdot 10^{-2}$ (m). The results are presented in the same way as for the simply supported plate, see Figure 20.

The penalty factor is set to $\alpha_{kl} = 10^3 \cdot E$ both for the penalty and the augmented lagrangian approach. An example of horizontal displacement is plotted for conforming meshes (top-left) and non-conforming meshes (top-right). We can see that, with a complete integration, these three methods exhibit the same solution as shown in the left plots. Concerning the reduced quadrature rule with an augmented approach, we observe that the reduced integration can lower the numerical locking. Moreover, the convergence rate for the finer meshes are quite similar for the complete and reduced quadrature rules. The developped reduced integration seems not as useful as for the plate due to the boundary conditions. In fact, the reduced quadrature rule is tuned for Dirichlet boundary conditions on all of the exterior edges. Consequently, when we have free edges, the quadrature rule is too restrictive, more details are given in [19]. Nevertheless, we will keep a reduced quadrature rule independent of the boundary conditions in order to be

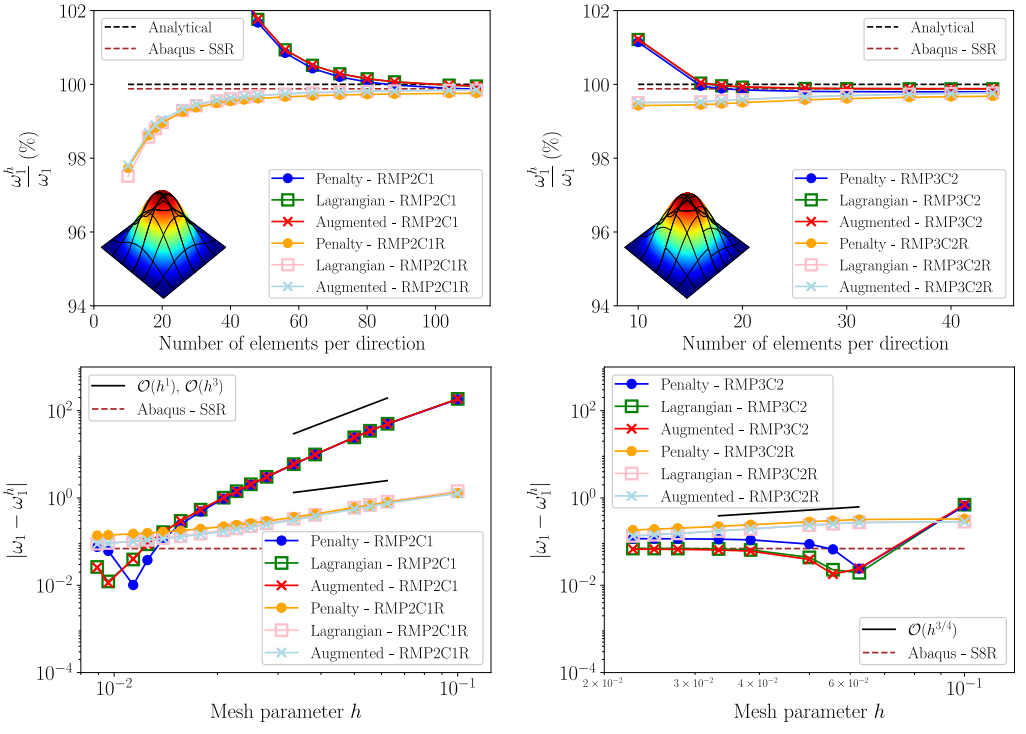

Figure 18: First eigenvalue for the clamped plate using the simplified mortar space. Left: quadratic functions. Right: cubic functions. Top: ratio w_1^h/w_1. Bottom: error $|w_1 - w_1^h|$.

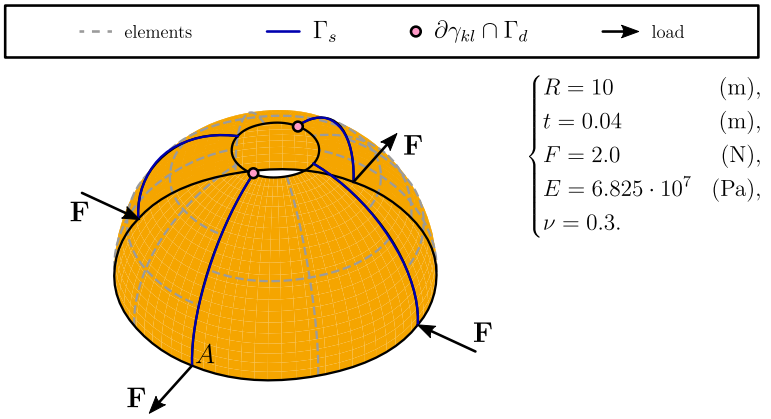

Figure 19: Geometry description and physical properties for a pinched hemisphere. Patches interface are represented in solid lines, elements in dotted lines.

robust on the industrial problems to follow at the potential cost of a small remaining locking.

7.3. Plate with hole

The last academic example considered herein is an "infinite plate", with a circular hole at its center, subjected to a uniformly distributed traction force of $T = F \cdot L = 10^5$ (N) far away. Using symmetry arguments, only a quarter of the plate will be considered. An analytical solution is given in [51, 55], predicting the value of σ_{xx} along the traction axis. However, this solution was given for 2D plane study with two DOF in translation for each control point. Consequently, using a thick plate element lead to an asymptotic difference of $4 \cdot 10^{-3}$ and therefore, we will take as a reference solution

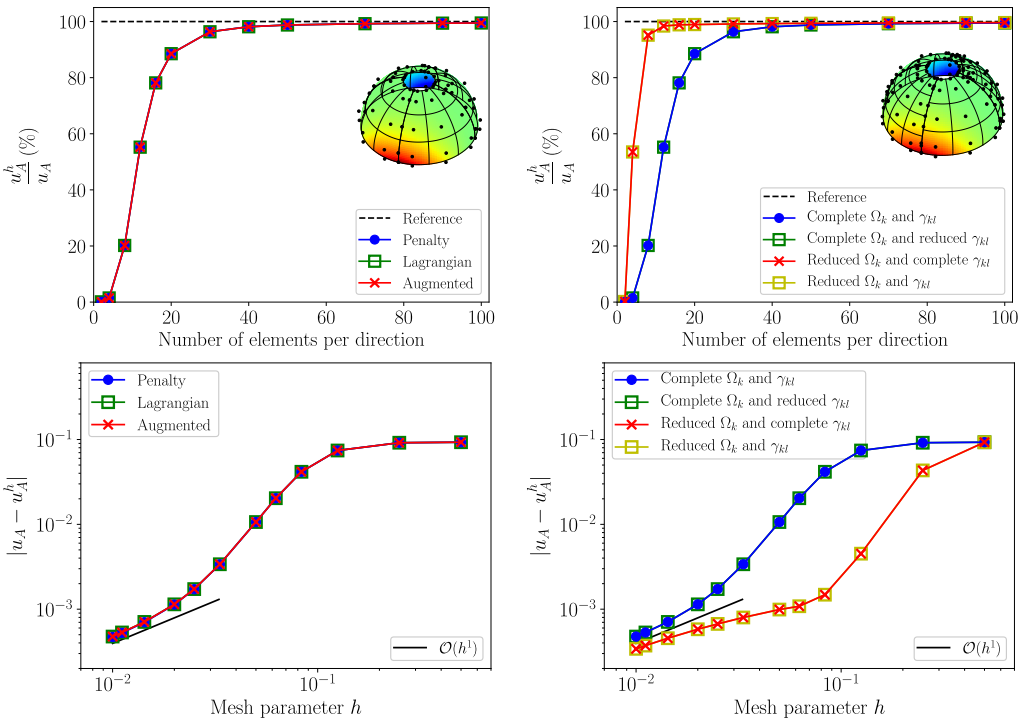

Figure 20: Displacement for the pinched hemisphere. Left: multipatch methods and complete integration using different formulations. Right: different quadrature rules using the same augmented lagrangian formulation.. Top: ratio u_A^h/u_A. Bottom: error $|u_A - u_A^h|$.

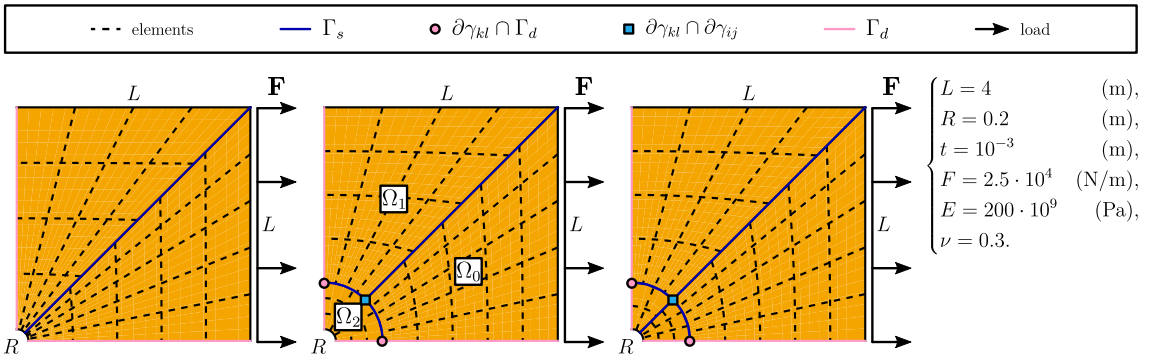

Figure 21: Geometry descriptions and physical properties for a plate with a hole. We present three partitions : the first one on the left uses two patches has no cross points. The middle one uses three patcches and is geometrically non-conforming with one cross point. The right one has four patches and is geometrically conforming with one cross point.

the one obtained for the two patch geometry using the finest mesh and fourth order NURBS (Figure 21).

For the partition represented on the left, the structure is made of two patches and no singular points are present. Obviously the simplified and optimal approaches will produce the same results. The two other parametrizations, which are on the center and on the right, have respectively three and four patches and present singular points coming from the boundary conditions and interfaces intersection. The parametrization with three patches have geometrically non-conforming interfaces whereas the four patches case only have geometrically conforming interfaces. The convergence

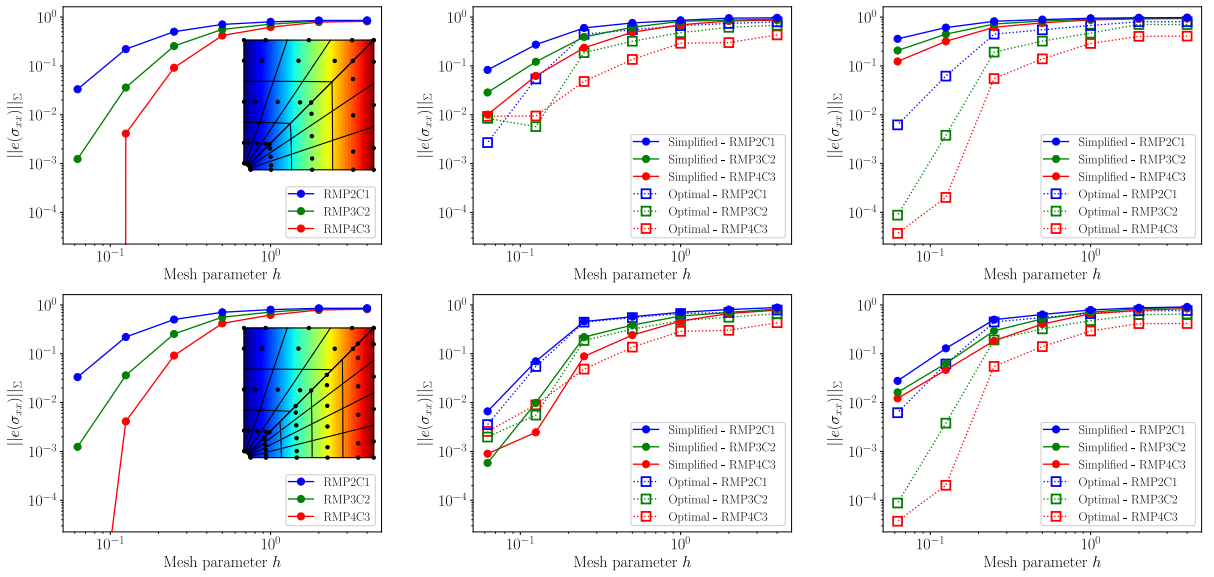

Figure 22: Simplified and optimal methods for the plate with hole. From left to right: parametrization with two, three and four patches. Top: dual approach. Bottom: augmented approach. We observe no major influence of the multipatch structure on the results accuracy.

will be studied using a broken L^2 norm on the stresses

$$||\sigma_{xx}||_\Sigma^2 = \sum_k ||\sigma_{xx}||^2_{L^2(\mathrm{Vol}_k)},$$

which is equivalent to a broken H^1 norm on the displacements. The relative error can then be computed as

$$||e(\sigma_{xx})||_\Sigma = \left| 1 - \frac{||\sigma_{xx} - \sigma^h_{xx}||_\Sigma}{||\sigma_{xx} - \sigma^{href}_{xx}||_\Sigma} \right|,$$

with σ^{href}_{xx} corresponding to the solution obtained with the two patch geometry using the finest mesh and fourth order NURBS.

This problem is locking free and thus we only show the results with complete integration. The results are shown on Figure 22 for the three parametrizations. Some examples of displacement along the traction axis are represented for the two patches case with conforming meshes (top-left) and non-conforming meshes (bottom-left). The penalty factor for the augmented approach is set to $\alpha_{kl} = 10 \cdot E/h$ in order to highlight the difference between optimal and simplified approaches depending on the mesh size.

Obviously, the simplified and optimal approaches produce the same results when the geometry is described with only two patches. However, when we have cross points, the optimal approach associated with a dual formulation keeps a smaller error than the simplified one. This was particularly expected because the dual space of the simplified method is not of optimal order with an additional term in $\sqrt{h}$. Nevertheless, when we add a regularization term, which corresponds to the bottom cases, the simplified and optimal methods have a similar convergence with our choice $\alpha_{kl} = 10 \cdot E/h$ of penalty factor. We note that a higher penalty factor could be used for the augmented approach with the simplified treatment at cross points associated with NURBS of order $p = 3$ and $p = 4$. The penalization term in the simplified approach is able to maintain the continuity constraint at cross points.

Concerning the geometrically non-conforming case, the solutions on Figure 22 are obtained by taking each of the three patches as the mortar side of at least an interface. For this balanced repartition we have respectively $\Omega_{s(10)} = \Omega_0$, $\Omega_{s(20)} = \Omega_2$ and $\Omega_{s(21)} = \Omega_1$ as the slave side for the interfaces γ_{10}, γ_{20} and γ_{21}. In order to show the robustness of the numerical implementation, we present on Figure 23 the errors obtained for the three patches parametrization with

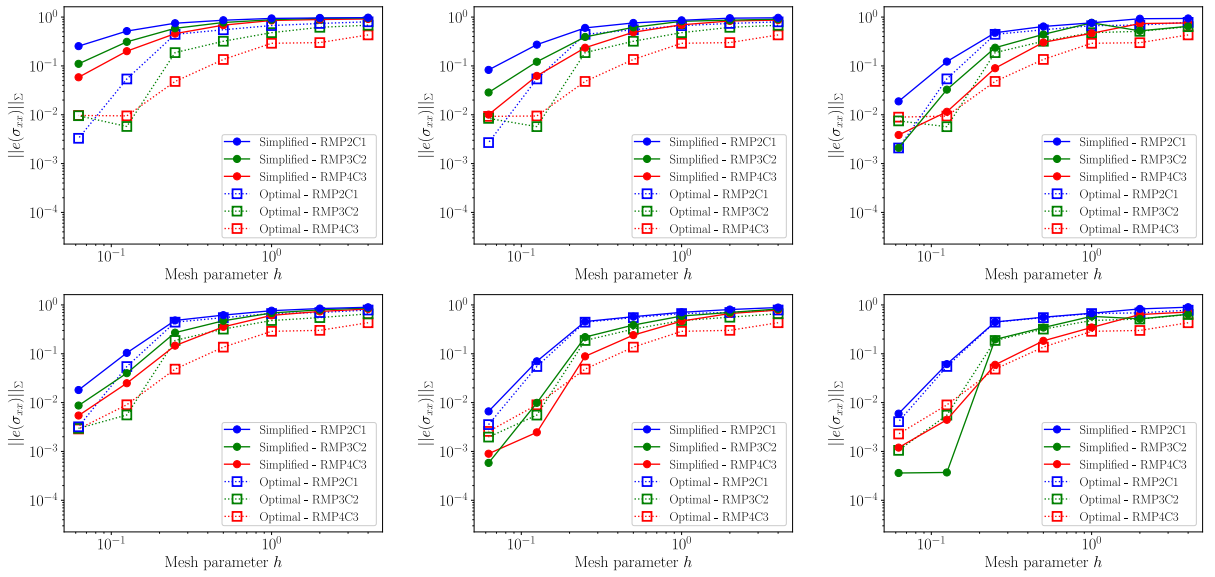

Figure 23: Different choices of mortar side for the three patches parametrization of the plate with hole. Left: geometrically slave conforming case ($\Omega_{s(10)} = \Omega_0$, $\Omega_{s(20)} = \Omega_0$ and $\Omega_{s(21)} = \Omega_1$). Center: balanced repartition of the slave side ($\Omega_{s(10)} = \Omega_0$, $\Omega_{s(20)} = \Omega_2$ and $\Omega_{s(21)} = \Omega_1$). Right: totally non-conforming case ($\Omega_{s(10)} = \Omega_0$, $\Omega_{s(20)} = \Omega_2$ and $\Omega_{s(21)} = \Omega_2$). Top: dual approach. Bottom: augmented approach. We observe no major influence of the choice of the mortar side on the results accuracy.

different choices of mortar side. On the left we have the geometrically slave conforming case which was the choice of [18]. The two plots at the center represent the balanced repartition. On the right, we took Ω_2 as the slave side for the two geometrically non-conforming interfaces γ_{20} and γ_{21}. We obtain similar convergence for the three different strategies. The industrial geometries to come will use a balanced repartition strategy for the mortar side.

7.4. Gear wheel

The following geometries are more complex and, therefore, no analytical solutions are available. Consequently, the discrete solutions obtained in IGA, with a simplified dual basis will be compared to a FEM one provided by Abaqus using thick shell elements. In a first step, the displacements are measured on the nodes of the FEM mesh. After solving a minimization problem, the corresponding parametric coordinates (ξ, η) are found and, thanks to the physical mapping $\mathbf{F}_k$, so are the physical coordinates. The displacement solutions can then be compared.

The first industrial geometry is a simplified gear wheel. In this case, all of the interfaces are geometrically conforming. The structure is clamped at its center and concentrated forces are applied on each tooth in such a way that we have an in-plane loading case, see Figure 24.

The global domain Ω was meshed using an homogeneous size of $h \simeq 0.1$ (m) for each patch Ω_k. The structure is made of 49 patches with 67 interfaces. We can visualize the horizontal displacements obtained using quadratic NURBS functions on Figure 25.

Using the same mesh for the FEM and IGA solutions, we can observe similar results between the augmented approach with reduced integrations and the numerical reference. We now want to compare the three multipatch formulations and quadrature rules. In order to do so, we plot the horizontal displacement along Γ_{obs} which is visible in green on Figure 24. These solutions are shown on Figure 26 for quadratic functions with complete and reduced integrations on the two top figures. The gaps between the solutions coming from IGA and these of FEM are shown on the bottom side. Penalty factors are set to $\alpha_{kl} = 10^3 \cdot E$ for displacements and rotations.

We can see that the element does not suffer from locking as we obtain the same results for complete and reduced integrations. However, we observe that when using the simplified space the dual method is less accurate than the augmented agrangian formulation because of the large number of cross points.

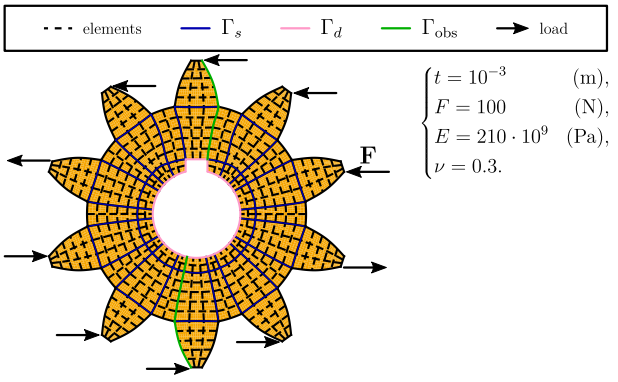

Figure 24: Geometry description and physical characteristics of the gear wheel. The partition uses 49 patches and 67 interfaces.

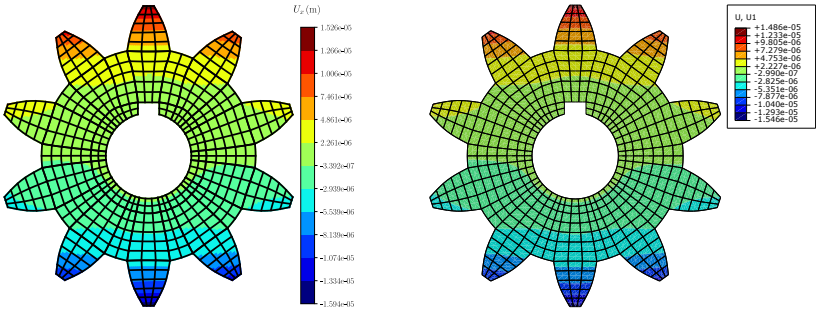

(a) IGA simplified augmented - RMP2C1R (b) FEM Abaqus - S8R

Figure 25: Horizontal displacement for the gear wheel problem.

7.5. Side rail

We are now considering a side rail taken from the automobile industry and modelled as a thick shell structure. As for the gear wheel, each interface is geometrically conforming (Figure 27).

The structure is made of 45 patches with 76 interfaces. A vertical constant pressure $\mathbf{F}$ is applied on three of the top surfaces. Two of its external edges, visible in pink on Figure 27, are clamped. We will compare results from IGA, with a mesh of 1946 quadratic elements, and FEM which will be our numerical reference with a fine mesh of 11 550 quadratic elements. The vertical displacement will be measured, as previously detailed, along the edge Γ_{obs}. At first, we visualize these displacements for both solutions on Figure 28.

After a qualitative validation between the dual approach with simplified mortar space and the FEM one, we compare the multipatch methods and quadrature rules on Figure 29. The left figures correspond to a complete integration whereas the right stand for the reduced quadrature rules. This study has highlighted a major drawback concerning the penalty method, that is the sensitivity to the choice of the penalty factor. Choosing $\alpha_{kl} = 10^3 \cdot E$ for the displacements and rotations lead to a lack of accuracy on the vertical displacements. Consequently, the penalty factors were set to $\alpha_{kl} \simeq 10^{-4} \cdot E$ for the displacements and $\alpha_{kl} \simeq E$ for the rotations when using the penalty method. For the augmented method, this choice was far less sensitive and therefore a unique penalty factor of $\alpha_{kl} = 10^{-5} \cdot E$ is used for both displacements and rotations .

We can see at first that the elements are suffering from numerical locking as the three multipatch formulations are not able to reach the reference when performing an exact integration. The reduced quadrature rule seems primordial when using quadratice NURBS for this kind of industrial problem. In constrast to the gear wheel problem, the dual approach using a simplified mortar space does not suffer from a lack of accuracy. This is due to the fact that we use a fine mesh and, consequently, the dual basis is rich enough even after removing the interpolating functions at cross points.

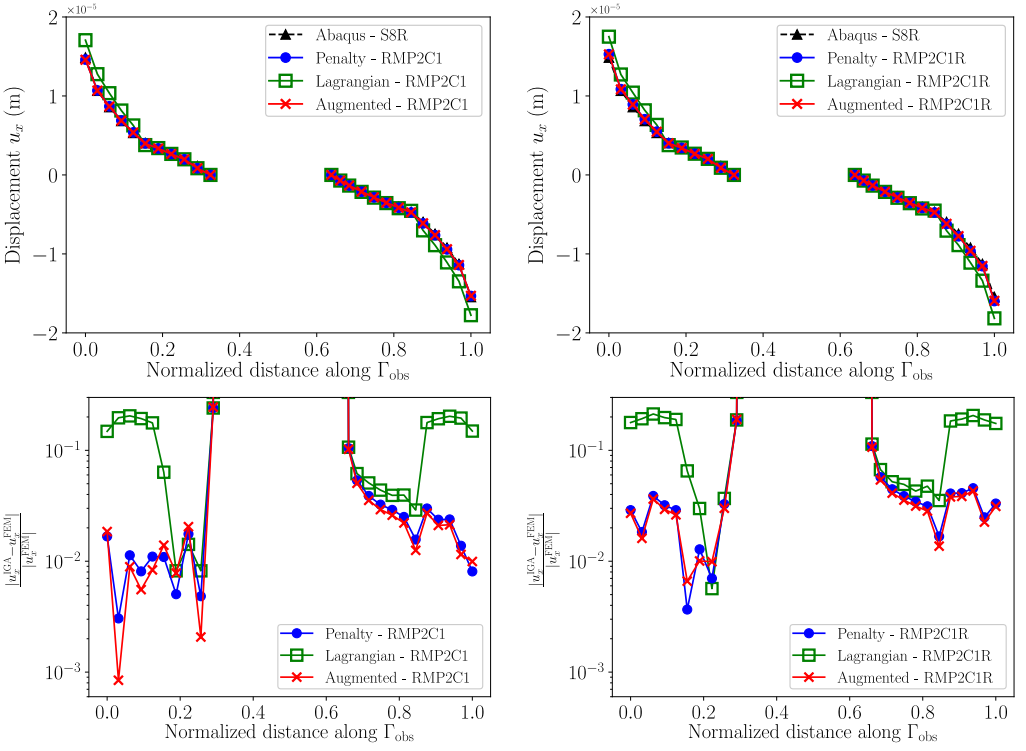

Figure 26: Displacement for the gear wheel. Left: complete integration. Right: reduced integration. Top: displacement u_x. Bottom: relative gap $|u_x^{\mathrm{IGA}} - u_x^{\mathrm{FEM}}| \,/\, |u_x^{\mathrm{FEM}}|$.

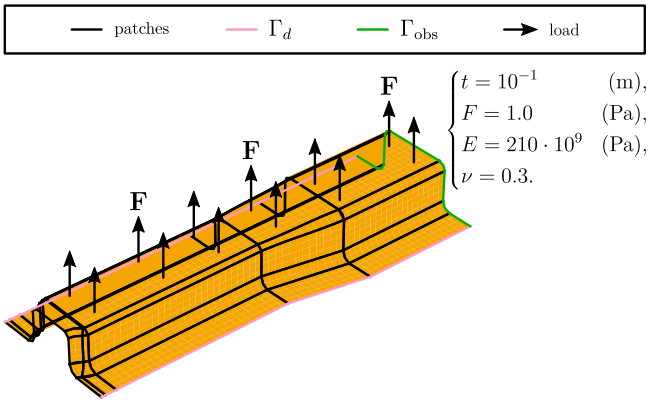

Figure 27: Geometry description and physical characteristics of the side rail. It is partitioned into 45 patches with 76 interfaces.

7.6. Oil sump

The last example is requiring more robustness, particularly for the creation of common knots vector on each interface. The structure is an oil sump for which the mid-surface has been extracted from a volumic part created in a CAD software. Its complexity justifies our preference for our simplified treatment of the cross points compared to an optimal construction which is hardly feasible here. This case presents many non geometrically conforming interfaces of different kinds as detailed in Remark 2. A description of the geometry, its patches and properties is given on Figure 30.

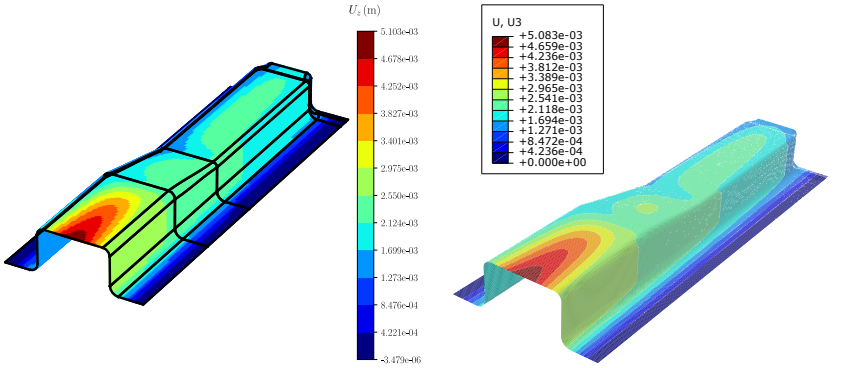

(a) IGA simplified dual - RMS2C1R (b) FEM Abaqus - S8R

Figure 28: Vertical displacement for the side rail problem.

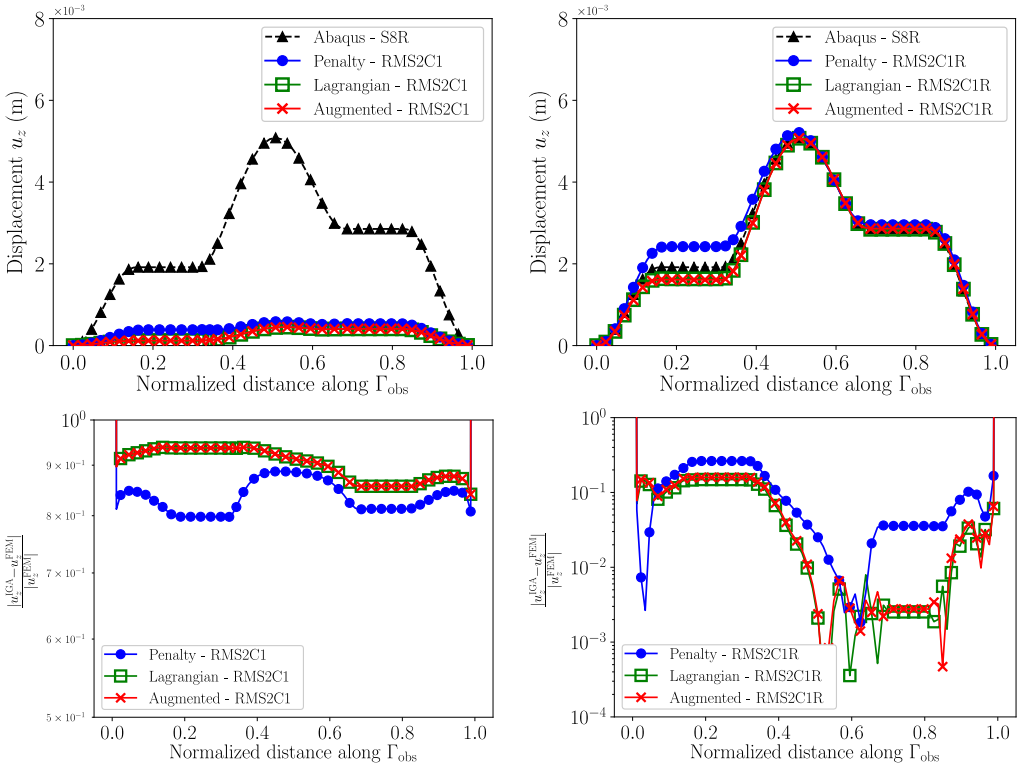

Figure 29: Displacement for the side rail. Left: complete integration. Right: reduced integration. Top: displacement u_z. Bottom: relative gap $|u_z^{\text{IGA}} - u_z^{\text{FEM}}| \,/\, |u_z^{\text{FEM}}|$.

This structure is made of 279 domains with 525 interfaces. A constant vertical pressure is applied on two of its upper surfaces and the bottom Γ_d is clamped. We will compare the penalty, the dual and the augmented lagrangian approach using the simplified mortar space and reduced integration. For the displacements and rotations, penalty factors are respectively fixed to $\alpha_{kl} = 10^3 \cdot E$ and $\alpha_{kl} = 10^{-5} \cdot E$ for the primal and augmented approaches. The vertical displacements can be observed on Figure 31 for both IGA and FEM solutions.

We are using 1047 (resp. 1570) quadratic elements for the two upper surfaces of the IGA (resp. FEM) mesh. We obtain similar results for the three approaches as seen on the values of the vertical displacements and horizontal

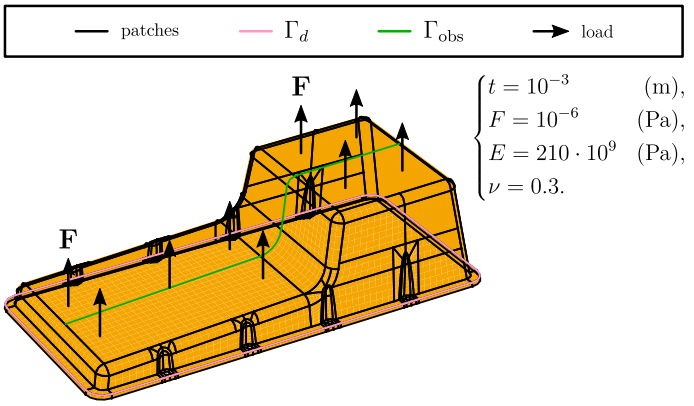

Figure 30: Geometry description and properties for an oil sump.

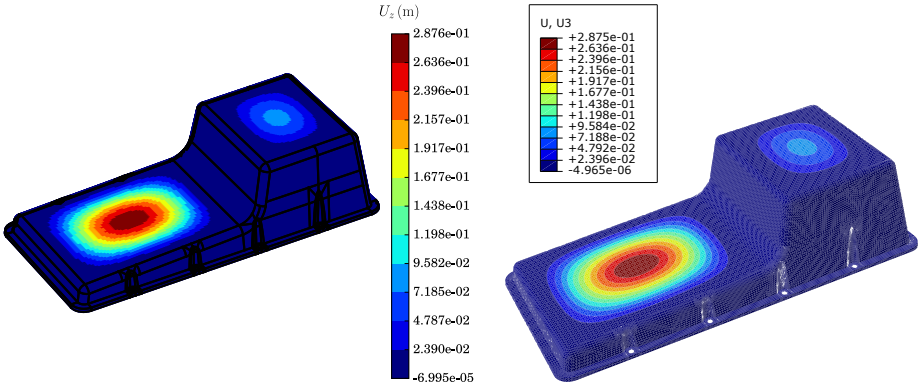

(a) IGA simplified augmented - RMS2C1R (b) FEM Abaqus - S8R

Figure 31: Vertical displacement for the oil sump problem.

rotations along Γ_{obs} (Figure 32). Despite of a coarser mesh for the IGA model, the displacements and rotations are similar to the numerical reference provided by Abaqus.

Remark 2. The oil sump contains many geometrically conforming and non-conforming interfaces. An illustration of the local complexity is given in Figure 33 representing the patch Ω_7 in the parameter space with its four interfaces represented by black lines. We can see three geometrically conforming situations with non-conforming meshes (a), hierarchical meshes (b) and conforming meshes (d). The situation (c) is geometrically non-conforming but with conforming meshes. Consequently, the common knots vectors Ξ^c are different, i.e., $\Xi^c_7 = \{0, 0.25, 0.5, 0.75, 1\}$ and $\Xi^c_{212} \simeq \{0, 0.08, 0.16, 0.25, 0.32\}$ respectively for Ω_7 and Ω_{212}. ■

8. Conclusion

In this paper, we have developed and analyzed a multipatch isogeometric analysis for thick shell structures, detailing proper choices of mortar spaces for imposing interpatch continuity and introducing an augmented lagrangian regularisation term for robustness. We have adapted the mortar space strategy proposed in [18] to the thick shell problem. It uses an equal order pairing taken from the primal basis and only require a local space reduction next to cross points. In order to handle complex situations encountered with real life industrial parts, we have proposed and assessed both theoretically and numerically a simpler correction removing interpolant basis functions at each end of an interface without any further modifications. The stability of the simplified approach was insured at the cost of a non optimal

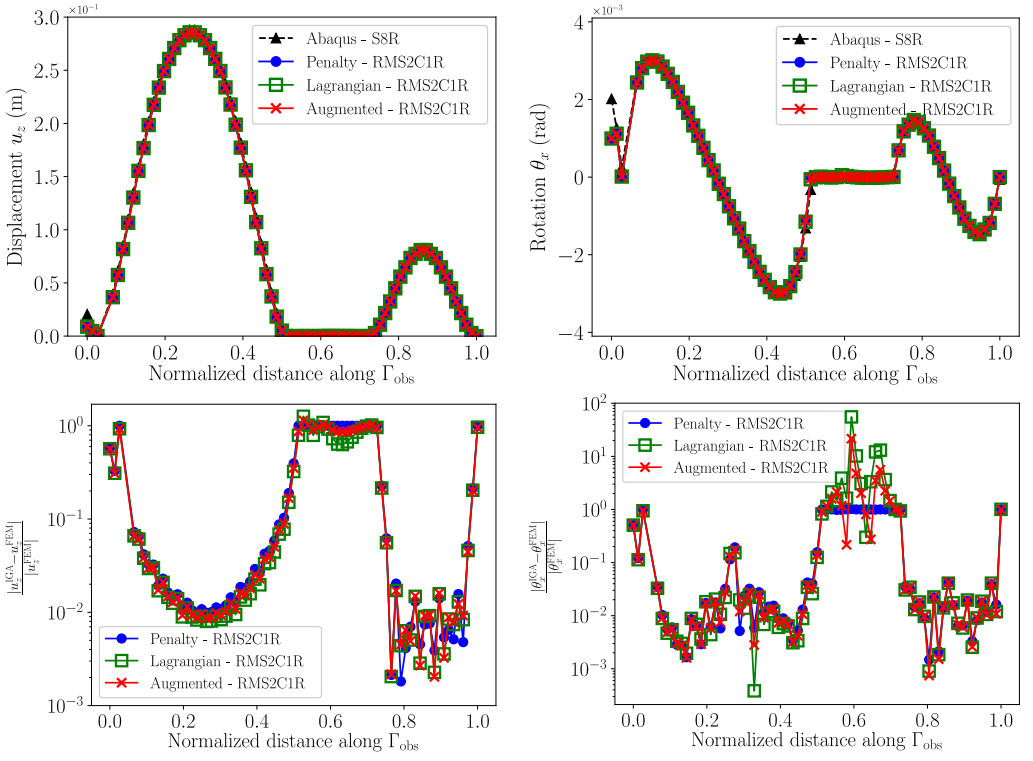

Figure 32: Solutions for the oil sump. Left: displacement u_z. Right: rotation θ_x. Top: displacement/rotation. Bottom: relative gap $|\{u_z/\theta_x\}^{\text{IGA}} - \{u_z/\theta_x\}^{\text{FEM}}| / |\{u_z/\theta_x\}^{\text{FEM}}|$.

order of convergence for the dual space. Nevertheless, adding a regularization term, which is the augmented method, is able to correct this lack of accuracy.

Altogether, combining this coupling strategy with an adequate reconstruction of surface normal through control vectors built at specific locations in the parametric space, and with the reduced quadrature rule proposed in [19] properly extended to a multipatch environment, we were able to handle a large variety of significant academic and industrial problems. It allowed us to significantly reduce the numerical locking without introducing any hourglass modes and this is particularly true for low order shape functions and coarse meshes. It also allowed us to solve complex problems with non geometrically conforming partitions, which are frequently encountered in practice, but which were rarely covered up to now in the literature. In particular, the technique seems well adapted to structures of moderate thickness, described with a large number of patches of moderate degree with many possibly non-conforming interfaces. This thus constitutes a promising way to introduce IGA in industrial applications.

Acknowledgments

This work was supported by the OpenLab Computational Mechanics created collectively by the Groupe PSA and the Laboratoire de Mécanique des Solides, École Polytechnique. This support is gratefully acknowledged.

References

[1] T.J.R. Hughes, J.A. Cottrell, Y. Bazilevs, Isogeometric analysis: CAD, finite elements, NURBS, exact geometry and mesh refinement, Computer Methods in Applied Mechanics and Engineering 194 (2005) 4135–4195.

[2] J.A. Cottrell, T.J.R. Hughes, Y. Bazilevs, Isogeometric Analysis: Toward Integration of CAD and FEA, Wiley, 2009.

[3] L. Piegl, W. Tiller, The $\mathcal{NURBS}$ Book, Springer-Verlag, Berlin, Heidelberg, 1995.

[4] M. Ruess, D. Schillinger, A.I. Özcan, E. Rank, Weak coupling for isogeometric analysis of non-matching and trimmed multi-patch geometries, Computer Methods in Applied Mechanics and Engineering 269 (2014) 46–71.

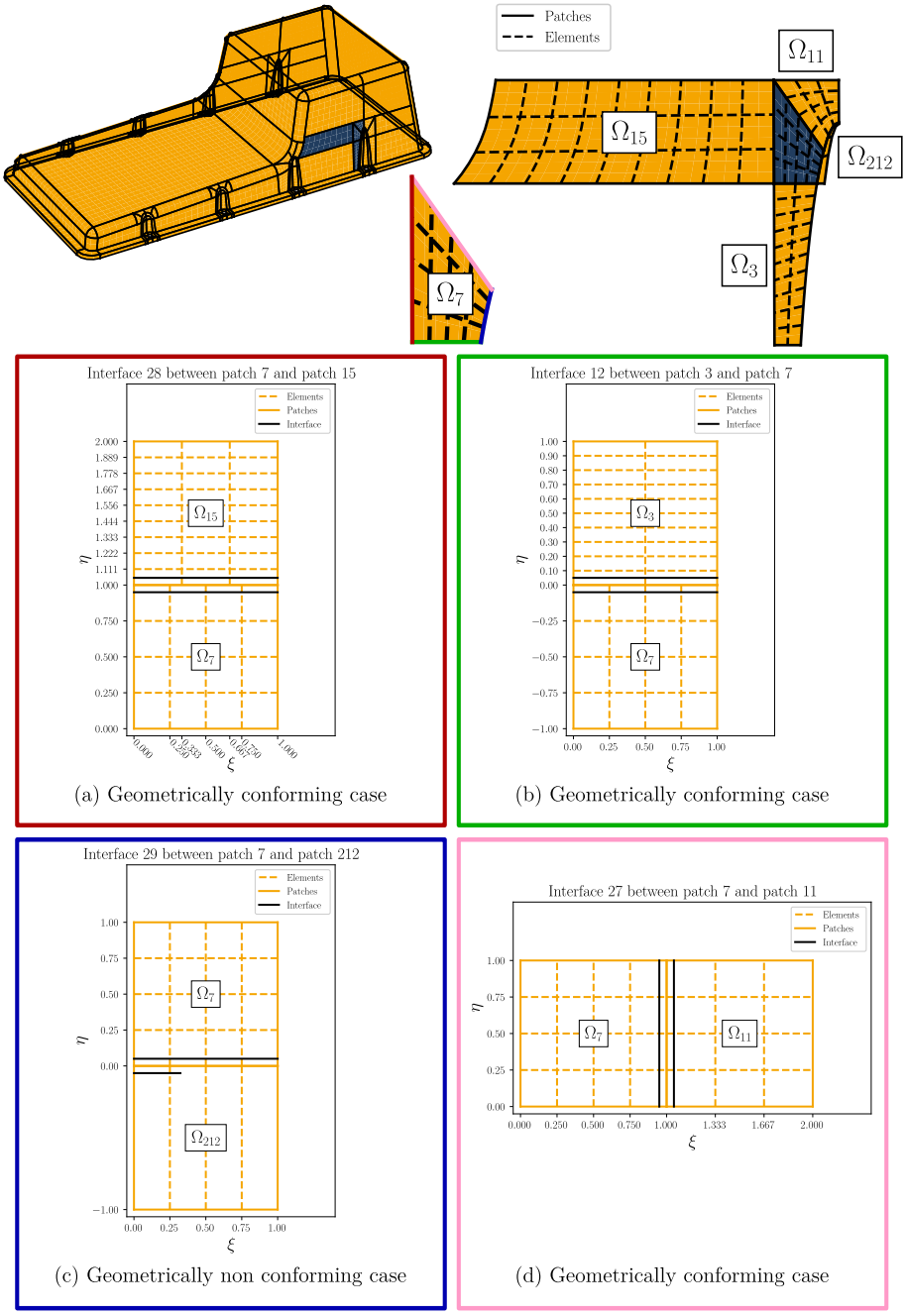

(a) Geometrically conforming case

(b) Geometrically conforming case

(c) Geometrically non conforming case

(d) Geometrically conforming case

Figure 33: Interfaces of patch Ω_7 in the parameter space for the oil sump.

[5] M. Breitenberger, A. Apostolatos, B. Philipp, R. Wüchner, K.-U. Bletzinger, Analysis in computer aided design: Nonlinear isogeometric B-Rep analysis of shell structures, Computer Methods in Applied Mechanics and Engineering 284 (2015) 401–457.

[6] Y. Guo, J. Heller, T.J.R. Hughes, M. Ruess, D. Schillinger, Variationally consistent isogeometric analysis of trimmed thin shells at finite deformations, based on the STEP exchange format, Computer Methods in Applied Mechanics and Engineering 336 (2018) 39–79.

[7] T. Teschemacher, A.M. Bauer, T. Oberbichler, M. Breitenberger, R. Rossi, R. Wüchner, K.-U. Bletzinger, Realization of CAD-integrated shell simulation based on isogeometric B-Rep analysis, Advanced Modeling and Simulation in Engineering Sciences 5 (2018) 19.

[8] J. Kiendl, Y. Bazilevs, M.-C. Hsu, R. Wüchner, K.-U. Bletzinger, The bending strip method for isogeometric analysis of Kirchhoff-Love shell structures comprised of multiple patches, Computer Methods in Applied Mechanics and Engineering 199 (2010) 2403–2416.

[9] E. Cohen, T. Lyche, R. Riesenfeld, Discrete B-splines and subdivision techniques in computer-aided geometric design and computer graphics, Computer Graphics and Image Processing 14 (1980) 87–111.

[10] Z. Lei, F. Gillot, L. Jezequel, A C^0/G^1 multiple patches connection method in isogeometric analysis, Applied Mathematical Modelling 39 (2015) 4405–4420.

[11] A. Apostolatos, R. Schmidt, R. Wüchner, K.-U. Bletzinger, A Nitsche-type formulation and comparison of the most common domain decomposition methods in isogeometric analysis, International Journal for Numerical Methods in Engineering 97 (2014) 473–504.

[12] V.P. Nguyen, P. Kerfriden, M. Brino, S.P.A. Bordas, E. Bonisoli, Nitsche's method for two and three dimensional NURBS patch coupling, Computational Mechanics 53 (2014) 1163–1182.

[13] L. De Lorenzis, P. Wriggers, G. Zavarise, A mortar formulation for 3D large deformation contact using NURBS-based isogeometric analysis and the augmented Lagrangian method, Computational Mechanics 49 (2012) 1–20.

[14] I. Temizer, P. Wriggers, T.J.R. Hughes, Three-dimensional mortar-based frictional contact treatment in isogeometric analysis with NURBS, Computer Methods in Applied Mechanics and Engineering 209-212 (2012) 115–128.

[15] J.-Y. Kim, S.-K. Youn, Isogeometric contact analysis using mortar method, International Journal for Numerical Methods in Engineering 89 (2012) 1559–1581.

[16] M. Dittmann, M. Franke, I. Temizer, C. Hesch, Isogeometric Analysis and thermomechanical Mortar contact problems, Computer Methods in Applied Mechanics and Engineering 274 (2014) 192–212.

[17] A. Seitz, P. Farah, J. Kremheller, B.I. Wohlmuth, W.A. Wall, A. Popp, Isogeometric dual mortar methods for computational contact mechanics, Computer Methods in Applied Mechanics and Engineering 301 (2016) 259–280.

[18] E. Brivadis, A. Buffa, B. Wohlmuth, L. Wunderlich, Isogeometric mortar methods, Computer Methods in Applied Mechanics and Engineering 284 (2015) 292–319.

[19] C. Adam, S. Bouabdallah, M. Zarroug, H. Maitournam, Improved numerical integration for locking treatment in isogeometric structural elements. Part II: Plates and shells, Computer Methods in Applied Mechanics and Engineering 284 (2015) 106–137.

[20] D.J. Benson, Y. Bazilevs, M.C. Hsu, T.J.R. Hughes, Isogeometric shell analysis: The Reissner-Mindlin shell, Computer Methods in Applied Mechanics and Engineering 199 (2010) 276–289.

[21] D.J. Benson, Y. Bazilevs, M.C. Hsu, T.J.R. Hughes, A large deformation, rotation-free, isogeometric shell, Computer Methods in Applied Mechanics and Engineering 200 (2011) 1367–1378.

[22] D. Chapelle, K.-J. Bathe, The Finite Element Analysis of Shells - Fundamentals. Second Edition, Springer-Verlag, Berlin, Heidelberg, 2011.

[23] F. Ben Belgacem, The mortar finite element method with Lagrange multipliers, Numerische Mathematik 84 (1999) 173–197.

[24] I. Babuška, The Finite Element Method with Lagrangian Multipliers, Numerische Mathematik 20 (1972) 179–192.

[25] F. Brezzi, M. Fortin, Mixed and Hybrid Finite Element Methods, Springer, 1991.

[26] F. Ben Belgacem, Y. Maday, The mortar element method for three dimensional finite elements, R.A.I.R.O. Modélisation Mathématique et Analyse Numérique 31 (1997) 289–302.

[27] A. Fritz, S. Hüeber, B.I. Wohlmuth, A comparison of mortar and Nitsche techniques for linear elasticity, Calcolo 41 (2004) 115–137.

[28] F. Brezzi, On the existence, uniqueness and approximation of saddle-point problems arising from lagrangian multipliers, R.A.I.R.O. Analyse Numérique 8 (1974) 129–151.

[29] K.-J. Bathe, The inf-sup condition and its evaluation for mixed finite element methods, Computers and Structures 79 (2001) 243–252.

[30] R. Glowinski, P. Le Tallec, Augmented Lagrangian and Operator-Splitting Methods in Nonlinear Mechanics, Studies in Applied and Numerical Mathematics, 1989.

[31] P. Le Tallec, T. Sassi, Domain Decomposition with Nonmatching Grids: Augmented Lagrangian Approach, Mathematics of Computation 64 (1995) 1367–1396.

[32] I. Babuška, The Finite Element Method with Penalty, Mathematics of Computation 27 (1973) 221–228.

[33] O.C. Zienkiewicz, R.L. Taylor, J.Z. Zhu, The Finite Element Method: Its Basis and Fundamentals (6^{th} edition), Elsevier, 2005.

[34] Y. Bazilevs, L. Beirão da Veiga, J.A. Cottrell, T.J.R. Hughes, G. Sangalli, Isogeometric Analysis: Approximation, stability and error estimates for h-refined meshes, Mathematical Models and Methods in Applied Sciences 16 (2006) 1031–1090.

[35] D. Braess, W. Dahmen, Stability Estimates of the Mortar Finite Element Method for 3-Dimensional Problems, East-West Journal of Numerical Mathematics 6 (1998) 249–263.

[36] D. Braess, W. Dahmen, C. Wieners, A Multigrid Algorithm For The Mortar Finite Element Method, SIAM Journal on Numerical Analysis 37 (1999) 48–69.

[37] B.I. Wohlmuth, A residual based error estimator for mortar finite element discretizations, Numerische Mathematik 84 (1999) 143–171.

[38] B.I. Wohlmuth, A Mortar Finite Element Method Using Dual Spaces for the Lagrange Multiplier, SIAM Journal on Numerical Analysis 38 (2000) 989–1012.

[39] D.S. Malkus, Eigenproblems associated with the discrete LBB condition for incompressible finite elements, International Journal of Engineering Science 19 (1981) 1299–1310.

[40] J.M. Melenk, B. Wohlmuth, Quasi-Optimal Approximation of Surface Based Lagrange Multipliers in Finite Element Methods, SIAM Journal on Numerical Analysis 50 (2012) 2064–2087.

[41] G. Farin, Curves and Surfaces for Computer-Aided Geometric Design. A Practical Guide, Fourth Edition, Academic Press, San Diego, 1997.

[42] T. Belytschko, W.K. Liu, B. Moran, Nonlinear Finite Elements for Continua and Structures, John Wiley & Sons, 2000.

[43] T.J.R. Hughes, The Finite Element Method: Linear Static and Dynamic Finite Element Analysis, Dover Publications, 2000.

[44] R. Echter, M. Bischoff, Numerical efficiency, locking and unlocking of NURBS finite elements, Computer Methods in Applied Mechanics and Engineering 199 (2010) 374–382.

[45] E. Rank, R. Krause, K. Preusch, On the accuracy of p-version elements for the Reissner Mindlin plate problem, International Journal for Numerical Methods in Engineering 43 (1998) 51–67.

[46] S.K. Lam, A. Pitrou, S. Seibert, Numba: A LLVM-based Python JIT Compiler, in: Proceedings of the Second Workshop on the LLVM

Compiler Infrastructure in HPC, LLVM '15, Association for Computing Machinery, New York, NY, USA, 2015, pp. 1–6.
[47] E. Jones, T. Oliphant, P. Peterson, SciPy: Open source scientific tools for Python, 2001.
[48] O. Schenk, K. Gärtner, W. Fichtner, A. Stricker, PARDISO: A High-performance Serial and Parallel Sparse Linear Solver in Semiconductor Device Simulation, Future Generation Computer Systems 18 (2001) 69–78.
[49] R.B. Lehoucq, D.C. Sorensen, C. Yang, ARPACK USERS GUIDE: Solution of Large Scale Eigenvalue Problems by Implicitly Restarted Arnoldi Methods, Society for Industrial and Applied Mathematics, Philadelphia, PA, USA, 1998.
[50] S. Timoshenko, S. Woinowsky-Krieger, Theory of Plates and Shells (Engineering Societies Monographs), Second Edition, McGraw-Hill College, 1959.
[51] P.L. Gould, Introduction to Linear Elasticity, Third Edition, Springer-Verlag, New York, 2013.
[52] C.M. Harris, A.G. Piersol, Harris' Shock and Vibration Handbook, McGraw-Hill, New York, 2002.
[53] T. Belytschko, H. Stolarski, W.K. Liu, N. Carpenter, J.S.-J. Ong, Stress projection for membrane and shear locking in shell finite elements, Computer Methods in Applied Mechanics and Engineering 51 (1985) 221–258.
[54] R.H. MacNeal, R.L. Harder, A proposed standard set of problems to test finite element accuracy, Finite Elements in Analysis and Design 1 (1985) 3–20.
[55] S. Timoshenko, J.N. Goodier, Theory of elasticity, McGraw-Hill, New York, 1951.

Supplementary material. Proof of lemma 2, not to be included in paper

Hereafter $(\cdot,\cdot)$ and $\|\cdot\|$ will denote the L^2 scalar product and norm on the interface γ_{kl}. The projection $\mathbf{w} = \mathbf{\Pi}_{kl,h}(\mathbf{v})$ is defined by

$$\min_{\hat{\mathbf{w}}\in W} \|\hat{\mathbf{w}} - \mathbf{v}\|^2 \text{ under the constraint } (\hat{\mathbf{w}}, \boldsymbol{\mu}) = (\mathbf{v}, \boldsymbol{\mu}), \forall \boldsymbol{\mu} \in M.$$

This is a coercive minimisation problem set on a closed subspace of W and has thus a unique solution. The corresponding Euler Lagrange optimality conditions are

$$\begin{aligned}
&(\mathbf{w} - \mathbf{v}, \hat{\mathbf{w}}) + (\hat{\mathbf{w}}, \lambda) = \mathbf{0}, \forall \hat{\mathbf{w}} \in W, \mathbf{w} \in W,\\
&(\mathbf{w}, \boldsymbol{\mu}) = (\mathbf{v}, \boldsymbol{\mu}), \forall \boldsymbol{\mu} \in M, \lambda \in M.
\end{aligned}$$

By application of the inf-sup assumption, there is a vector $\mathbf{w}_\lambda \in W$ such that $(\mathbf{w}_\lambda, \lambda) \geq C\|\mathbf{w}_\lambda\|\|\lambda\|$. Using this vector as a test function in the first equality, we get

$$\|\mathbf{w}_\lambda\|\|\lambda\| \leq \frac{1}{C}(\mathbf{w}_\lambda, \lambda) = -\frac{1}{C}(\mathbf{w} - \mathbf{v}, \mathbf{w}_\lambda) \leq \frac{1}{C}\|\mathbf{w} - \mathbf{v}\|\|\mathbf{w}_\lambda\|$$

hence after division

$$\|\lambda\| \leq \frac{1}{C}\|\mathbf{w} - \mathbf{v}\|.$$

Plugging this in the first equality written with $\hat{\mathbf{w}} = \mathbf{w}$ and in the second equality writtten with $\boldsymbol{\mu} = \lambda$ yields

$$\|\mathbf{w} - \mathbf{v}\|^2 = -(\mathbf{w} - \mathbf{v}, \mathbf{v}) - (\mathbf{w}, \lambda) = -(\mathbf{w} - \mathbf{v}, \mathbf{v}) - (\mathbf{v}, \lambda) \leq \|\mathbf{v}\|(\|\mathbf{w} - \mathbf{v}\| + \|\lambda\|) \leq (\frac{1}{C} + 1)\|\mathbf{v}\|\|\mathbf{w} - \mathbf{v}\|$$

hence after division $\|\mathbf{w}-\mathbf{v}\|$ is bounded by $\|\mathbf{v}\|$ which yields the desired result by application of the triangular inequality.

Detailed conclusion of proof of Proposition 4, not to be included in paper

By construction of $\mathbf{v}_h = \left\{(\mathbf{v}_p)_h, \boldsymbol{\vartheta}_h\right\} \in \mathrm{Ker}(\mathbf{C}_h)$, their interface jumps are orthogonal to the dual interface spaces, and hence, by introducing L^2 projections $\boldsymbol{\mu}_{kl,h}$ of λ_k onto $M_{kl,h}$, we get

$$a(\mathbf{u}, \mathbf{v}_h) - L(\mathbf{v}_h) = \sum_{k>l} \int_{\gamma_{kl}} (\lambda_k - \boldsymbol{\mu}_{kl,h}) \cdot (\mathbf{v}_{k,h} - \mathbf{v}_{l,h}) \, \mathrm{d}\gamma_{kl}.$$

In turn, $\lambda_k - \boldsymbol{\mu}_{kl,h}$ is orthogonal by construction to any function $\hat{\boldsymbol{\mu}}_{kl,h}$ in $M_{kl,h}$, and hence

$$a(\mathbf{u}, \mathbf{v}_h) - L(\mathbf{v}_h) = \sum_{k>l} \int_{\gamma_{kl}} (\lambda_k - \boldsymbol{\mu}_{kl,h}) \cdot (\mathbf{v}_{k,h} - \mathbf{v}_{l,h} - \hat{\boldsymbol{\mu}}_{kl,h}) \, \mathrm{d}\gamma_{kl}.$$

From Assumption 4, we have on one hand (assuming that k is the slave node of kl)

$$||\lambda_k - \boldsymbol{\mu}_{kl,h}||_{L^2(\gamma_{kl})^2} = \inf_{\hat{\boldsymbol{\mu}}_{kl,h}\in M_{kl,h}} ||\lambda_k - \hat{\boldsymbol{\mu}}_{kl,h}||_{L^2(\gamma_{kl})^2} \leq C h_{kl}^s ||\lambda_k||_{H^s(\gamma_{kl})^2} \leq C h_k^s ||\mathbf{u}_k||_{H^{s+3/2}(\Omega_k)^2},$$

for any $0 < s \leq \eta(kl)$ and on the other hand

$$\begin{aligned}\inf_{\hat{\boldsymbol{\mu}}_{kl,h}\in M_{kl,h}} ||\mathbf{v}_{k,h} - \mathbf{v}_{l,h} - \hat{\boldsymbol{\mu}}_{kl,h}||_{L^2(\gamma_{kl})^2} &\leq \inf_{\hat{\boldsymbol{\mu}}_{kl,h}\in M_{kl,h}} ||\mathbf{v}_{k,h} - \hat{\boldsymbol{\mu}}_{kl,h}||_{L^2(\gamma_{kl})^2} + \inf_{\hat{\boldsymbol{\mu}}_{kl,h}\in M_{kl,h}} ||\mathbf{v}_{l,h} - \hat{\boldsymbol{\mu}}_{kl,h}||_{L^2(\gamma_{kl})^2} \\ &\leq C\sqrt{h_{kl}}(||\mathbf{v}_{k,h}||_{H^{1/2}(\gamma_{kl})^2} + ||\mathbf{v}_{l,h}||_{H^{1/2}(\gamma_{kl})^2}).\end{aligned}$$

Altogether, we get after summation and using Cauchy Schwarz

$$\begin{aligned}a(\mathbf{u}, \mathbf{v}_h) - L(\mathbf{v}_h) &\leq \sum_{kl} C h_k^r ||\mathbf{u}||_{H^{r+1}(\Omega_k)^2}(||\mathbf{v}_{k,h}||_{H^1(\Omega_k)^2} + ||\mathbf{v}_{l,h}||_{H^1(\Omega_k)^2}) \\ &\leq C\sqrt{\sum_k h_k^{2r}||\mathbf{u}||^2_{H^{r+1}(\Omega_k)^2}}\sqrt{\sum_k ||\mathbf{v}_{k,h}||^2_{H^1(\Omega_k)^2}}\end{aligned}$$

with $1/2 < r \leq \min_{kl}(\eta(kl) + 1/2)$. ■

Supplementary material. Detailed proof of Proposition 5, not to be included in paper

We need to estimate $||\mathbf{E}_{kl,h}\circ\boldsymbol{\Pi}_{kl,h}\left[\mathbf{I}_h(\mathbf{u})\right]||_{\Pi H^1(\Omega_k)^2}$ where $\mathbf{E}_{kl,h}$ is the zero extension of an element of $W_{kl,h}$. We denote $\tilde{\mathbf{Q}}$ and $\mathbf{Q}$ the quadrangular finite elements in the parent space and in the physical space, respectively. Since all norms are equivalent on the reference element $\tilde{\mathbf{Q}}$, we have

$$||\tilde{\boldsymbol{\nabla}}\mathbf{E}_{kl,h}\circ\boldsymbol{\Pi}_{kl,h}\left[\mathbf{I}_h(\mathbf{u})\right]||^2_{L^2(\tilde{\mathbf{Q}})^2} \leq C||\boldsymbol{\Pi}_{kl,h}\left[\mathbf{I}_h(\mathbf{u})\right]||^2_{L^2(\partial\tilde{\mathbf{Q}}\cap\tilde{\gamma}_{kl})^2},$$

with $\tilde{\gamma}_{kl}$ the kl interface once transported on the parent element. After change of variable, since $\boldsymbol{\nabla}\mathbf{E}_{kl,h} = \dfrac{1}{h_k}\tilde{\boldsymbol{\nabla}}\mathbf{E}_{kl,h}$ and $\mathrm{d}\mathbf{Q} = h_k^2\,\mathrm{d}\tilde{\mathbf{Q}}$, we have

$$||\tilde{\boldsymbol{\nabla}}\mathbf{E}_{kl,h}\circ\boldsymbol{\Pi}_{kl,h}\left[\mathbf{I}_h(\mathbf{u})\right]||^2_{L^2(\tilde{\mathbf{Q}})^2} \simeq ||\boldsymbol{\nabla}\mathbf{E}_{kl,h}\circ\boldsymbol{\Pi}_{kl,h}\left[\mathbf{I}_h(\mathbf{u})\right]||^2_{L^2(\mathbf{Q})^2},$$

yielding

$$\begin{aligned}||\boldsymbol{\nabla}\mathbf{E}_{kl,h}\circ\boldsymbol{\Pi}_{kl,h}\left[\mathbf{I}_h(\mathbf{u})\right]||^2_{L^2(\mathbf{Q})^2} &\leq C||\boldsymbol{\Pi}_{kl,h}\left[\mathbf{I}_h(\mathbf{u})\right]||^2_{L^2(\partial\tilde{\mathbf{Q}}\cap\tilde{\gamma}_{kl})^2} \\ &\leq \frac{C}{h_k}||\boldsymbol{\Pi}_{kl,h}\left[\mathbf{I}_h(\mathbf{u})\right]||^2_{L^2(\partial\mathbf{Q}\cap\gamma_{kl})^2}.\end{aligned}$$

After summation and using the L^2 continuity of the projector $\boldsymbol{\Pi}_{kl,h}$ (Lemma 2), this gives

$$\begin{aligned}||\mathbf{E}_{kl,h}\circ\boldsymbol{\Pi}_{kl,h}\left[\mathbf{I}_h(\mathbf{u})\right]||_{H^1(\Omega_k)^2} &\leq \frac{C}{\sqrt{h_k}}||\left[\mathbf{I}_h(\mathbf{u})\right]||_{L^2(\gamma_{kl})^2} \\ &\leq \frac{C}{\sqrt{h_k}}||\left[\mathbf{u} - \mathbf{I}_h(\mathbf{u})\right]||_{L^2(\gamma_{kl})^2} \\ &\leq \frac{C}{\sqrt{h_k}}\left(||\mathbf{u}_k - \mathbf{I}_h(\mathbf{u}_k)||_{L^2(\gamma_{kl})^2} + ||\mathbf{u}_l - \mathbf{I}_h(\mathbf{u}_l)||_{L^2(\gamma_{kl})^2}\right).\end{aligned}$$

We now conclude by a classical scaling argument of Finite Element analysis, although there might be a better proof in the spline community. Let us thus look as in [36] to the approximation error on an element γ^e of the mesh of γ_{kl}. By construction, once pulled back on the parametric space of the k patch properly dilated so that the image $\hat{\gamma}$ of γ^e be of unit length, the map $\hat{\mathbf{I}}_h(\hat{\mathbf{v}}) - \hat{\mathbf{v}}$ used in Lemma 1 is continuous from $L^2(\hat{Q})$ onto $L^2(\hat{\gamma})$ and hence from $H^{r+1}(\hat{Q})$ onto $L^2(\hat{\gamma})$, where $\hat{Q}$ is a fixed mesh independent domain, which is the union of all mesh elements in the parametric

space which are used for the construction of $\hat{\mathbf{I}}_h(\hat{\mathbf{v}})$. We also observe that the approximation is exact for polynomials of degree r on $\hat{Q}$

$$\hat{\mathbf{I}}_h(\hat{\mathbf{q}}) - \hat{\mathbf{q}} = \mathbf{0}, \forall \hat{\mathbf{q}} \in P^r(\hat{Q}).$$

By continuity of the map, there exists therefore a mesh independent constant such that

$$\|\hat{\mathbf{I}}_h(\hat{\mathbf{v}}) - \hat{\mathbf{v}}\|_{L^2(\hat{\gamma})} = \|\hat{\mathbf{I}}_h(\hat{\mathbf{v}} - \hat{\mathbf{q}}) - (\hat{\mathbf{v}} - \hat{\mathbf{q}})\|_{L^2(\hat{\gamma})} \leq \inf_{\mathbf{q} \in P^r(\hat{Q})} \|\hat{\mathbf{v}} - \hat{\mathbf{q}}\|_{H^{r+1}(\hat{Q})} \leq C|\hat{\mathbf{v}}|_{H^{r+1}(\hat{Q})}, \forall \hat{\mathbf{v}} \in H^{r+1}(\hat{Q}).$$

By going back to the physical space, and since from the regularity of $\mathbf{F}_k$, the norm in $L^2(\gamma^e)$ scales in $\sqrt{h_k}$ while the semi norm in $H^{r+1}(Q)$ scales in h_k^{-r}, we obtain that

$$||\mathbf{v}_k - \mathbf{I}_h(\mathbf{v}_k)||^2_{L^2(\gamma^e)^2} \leq C^2 h_k^{2r+1/2} \sum_{Q \subset Q^e} |\mathbf{v}|^2_{H^{r+1}(Q)^2}.$$

By summation, and since a given element Q will only be involved an $\mathcal{O}(p)$ number of times for constructing local approximation on segments γ^e, we have

$$||\mathbf{v}_k - \mathbf{I}_h(\mathbf{v}_k)||^2_{L^2(\gamma_{kl})^2} \leq \sum_e ||\mathbf{v}_k - \mathbf{I}_h(\mathbf{v}_k)||^2_{L^2(\gamma^e)^2} \leq C h_k^{2r+1/2} \sum_e \sum_{Q \subset Q^e} |\mathbf{v}|^2_{H^{r+1}(Q)^2} \leq C h_k^{2r+1/2} |\mathbf{v}|^2_{H^{r+1}(\Omega_k)^2}.$$

By using this inequality in our previous estimate, we get

$$||\mathbf{E}_{kl,h} \circ \mathbf{\Pi}_{kl,h} \left[\mathbf{I}_h(\mathbf{u})\right]||_{H^1(\Omega_k)^2} \leq \frac{C}{\sqrt{h_k}} \left(h_k^{r+1/2} ||\mathbf{u}_k||_{H^{r+1}(\Omega_k)^2} + h_l^{r+1/2} ||\mathbf{u}_l||_{H^{r+1}(\Omega_l)^2} \right)$$

which yields the desired result, once combined with Lemma 1.